Geoscience Frontiers 10 (2019) 2153–2166

HOSTED BY

ELSEVIER

Contents lists available at ScienceDirect

China University of Geosciences (Beijing)

Geoscience Frontiers

journal homepage: www.elsevier.com/locate/gsf

Research Paper

Thermo-tectonic history of the Junggar Alatau within the Central Asian Orogenic Belt (SE Kazakhstan, NW China): Insights from integrated apatite U/Pb, fission track and (U–Th)/He thermochronology

S. Glorie [a,*], A. Otasevic [a], J. Gillespie [a], G. Jepson [a,b], M. Danišík [c], F.I. Zhimulev [d], D. Gurevich [e], Z. Zhang [f], D. Song [f], W. Xiao [f,g]

[a] Department of Earth Sciences, School of Physical Sciences, The University of Adelaide, SA 5005, Australia
[b] Department of Geosciences, University of Arizona, Tucson, AZ, USA
[c] John de Laeter Centre, TIGeR, Curtin University, WA 6846, Australia
[d] Sobolev Institute of Geology and Mineralogy, Siberian Branch of the Russian Academy of Sciences, 2 Pirogova St., Novosibirsk 630090, Russia
[e] SRK Exploration, Moscow, Russia
[f] State Key Laboratory of Lithospheric Evolution, Institute of Geology and Geophysics, Chinese Academy of Sciences, Beijing 100029, China
[g] Xinjiang Research Centre for Mineral Resources, Xinjiang Institute of Ecology and Geography, Chinese Academy of Sciences, Urumqi 830011, China

ARTICLE INFO

Article history:
Received 25 February 2019
Received in revised form
28 April 2019
Accepted 23 May 2019
Available online 31 May 2019
Handling Editor: M. Santosh

Keywords:
Junggar
Central Asian Orogenic Belt
Thermochronology
Exhumation
Fault reactivation
Tethys

ABSTRACT

The Junggar Alatau forms the northern extent of the Tian Shan within the Central Asian Orogenic Belt (CAOB) at the border of SE Kazakhstan and NW China. This study presents the Palaeozoic–Mesozoic post-collisional thermo-tectonic history of this frontier locality using an integrated approach based on three apatite geo-/thermochronometers: apatite U–Pb, fission track and (U–Th)/He. The apatite U–Pb dates record Carboniferous–Permian post-magmatic cooling ages for the sampled granitoids, reflecting the progressive closure of the Palaeo-Asian Ocean. The apatite fission track (AFT) data record (partial) preservation of the late Palaeozoic cooling ages, supplemented by limited evidence for Late Triassic (~230–210 Ma) cooling and a more prominent record of (late) Early Cretaceous (~150–110 Ma) cooling. The apatite (U–Th)/He age results are consistent with the (late) Early Cretaceous AFT data, revealing a period of fast cooling at that time in resulting thermal history models. This Cretaceous rapid cooling signal is only observed for samples taken along the major NW–SE orientated shear zone that dissects the study area (the Central Kazakhstan Fault Zone), while Permian and Triassic cooling signals are preserved in low-relief areas, distal to this structure. This distinct geographical trend with respect to the shear zone, suggests that fault reactivation triggered the Cretaceous rapid cooling, which can be linked to a phase of slab-rollback and associated extension in the distant Tethys Ocean. Similar conclusions were drawn for thermochronology studies along other major NW–SE orientated shear zones in the Central Asian Orogenic Belt, suggesting a regional phase of Cretaceous exhumation in response to fault reactivation at that time.

1. Introduction

The Junggar Alatau represents the western extent of the northern Chinese Tian Shan that is located within the larger Central Asian Orogenic Belt (CAOB) (Fig. 1). The CAOB represents a vast accretionary orogen that was formed during the Palaeozoic (Windley et al., 2007; Choulet et al., 2012) and became reactivated during the Meso-Cenozoic (e.g. Glorie and De Grave, 2016). In this time period, the CAOB experienced intracontinental deformation associated with distant tectonic events that transpired during the consumption of the former Tethys Ocean (e.g. De Grave et al., 2007; Glorie et al., 2010) and Mongol-Okhotsk Ocean (e.g. Jolivet et al., 2009; Glorie et al., 2012a). Stress-fields as a result of these distal tectonic events propagated through the inherited Palaeozoic structures of the CAOB resulting in the progressive and punctuated exhumation and mountain building events that shaped the

* Corresponding author.
E-mail address: stijn.glorie@adelaide.edu.au (S. Glorie).
Peer-review under responsibility of China University of Geosciences (Beijing).

https://doi.org/10.1016/j.gsf.2019.05.005

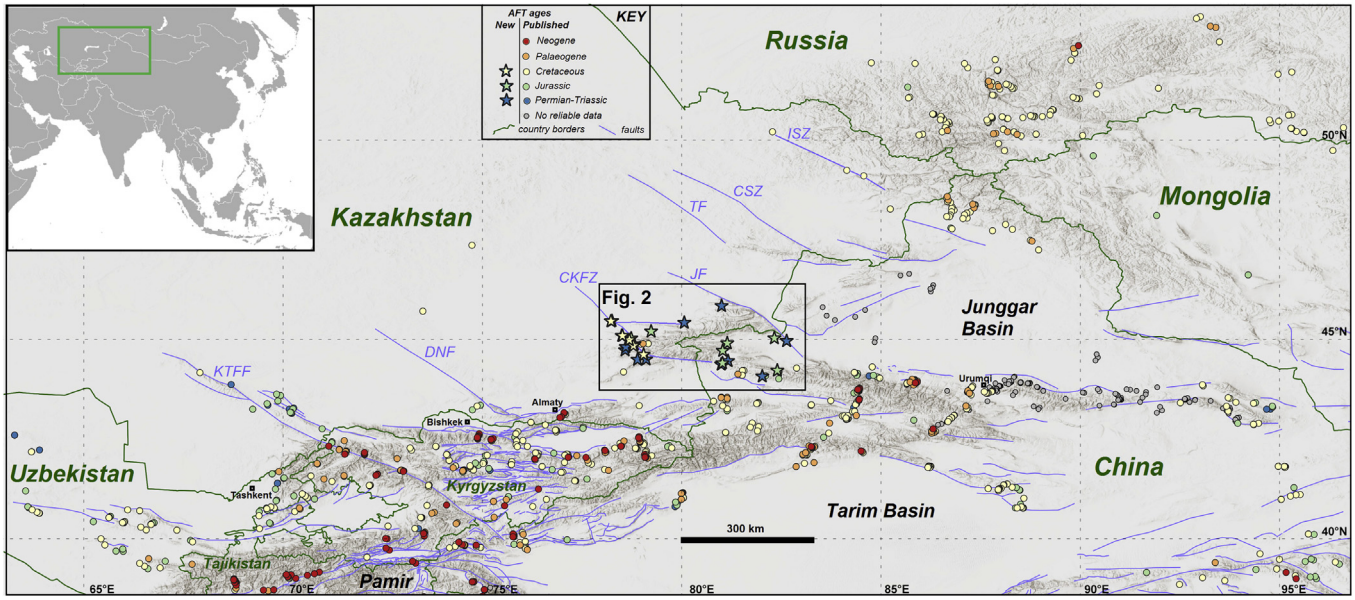

Fig. 1. Digital elevation model of Central Asia with colour-coded annotations of published AFT ages (circle symbols) and new AFT ages (star symbols). Published AFT ages were sourced from Dumitru et al. (2001); Jolivet et al. (2001, 2010); De Grave and Van den haute (2002); Guo et al. (2006); Sobel et al. (2006a, b); Yuan et al. (2006); De Grave et al. (2007, 2008, 2011, 2012, 2013, 2014); Du et al. (2007); Zhang et al. (2007, 2009, 2016); Wang et al. (2009, 2018b); Glorie et al. (2010, 2011, 2012a, b); Macaulay et al. (2014); Yang et al. (2014); Bande et al. (2015, 2017); De Pelsmaeker et al. (2015); Tang et al. (2015); Käßner et al. (2016); Gillespie et al. (2017a, b); Rutte et al. (2017); Jepson et al. (2018a, b, c); Nachtergaele et al. (2018); Song et al. (2018); Jepson et al. (2019). Sample locations with doubtful data (anomalously young AFT ages) are displayed by gray symbols (see e.g. Gillespie et al., 2017a; Nachtergaele et al., 2018 for more information). The study area in the Junggar-Alatau is outlined by the black box. Inset = overview map of Central Asia. The fault outlines were adapted from the Central Asia Fault Database (Mohadjer et al., 2015). The most prominent NW–SE striking shear zones that dissect the Central Asian Orogenic Belt, to south of the Altai, are named on the map, with: KTFF = Karatau-Talas-Ferghana Fault, DNF = Dzhalair-Naiman Fault, CKFZ = Central Kazakhstan Fault Zone, JF = Junggar Fault, TF = Tarbagatay Fault, CSZ = Chara Shear zone, ISZ = Irtysh Shear Zone.

prominent Tian Shan (e.g. Jolivet et al., 2010; Glorie et al., 2011; Macaulay et al., 2014; Jepson et al., 2018c) and Altai-Sayan (e.g. De Grave et al., 2008; Glorie et al., 2012a; De Grave et al., 2014) mountainous landscapes that are seen today. The Junggar Alatau forms a key region at the frontier of these two orogens (Fig. 1), where in comparison to the Tian Shan and Altai, thermochronological data is largely lacking. Studying the thermal history of such areas is important as it is likely that they record less Cenozoic deformation overprint given their lower mean elevation, and it is thus more likely that they preserve an archive of Mesozoic thermo-tectonic events. In this regard, limited previous work by in the Junggar Alatau study area by De Pelsmaeker et al. (2015) and Wang et al. (2018b) revealed mostly Cretaceous apatite fission track (AFT) cooling ages (Fig. 1) that reflect slow cooling at that time. However, a systematic thermochronological study that particularly targets the main NW–SE fault zone that dissects the Junggar Alatau (the Central Kazakhstan Fault Zone or CKFZ) (Figs. 1 and 2) has not been carried out.

Previous studies across Central Asia have shown that major NW–SE orientated shear zones, such as the prominent Talas-Fergana and Irtysh shear zones (Fig. 1), record thermal histories of rapid cooling during the late Cretaceous (e.g. Glorie et al., 2012b; Nachtergaele et al., 2018). This study aims to test whether the CKFZ, which runs parallel to the Irtysh and Talas-Fergana shear zones, records a similar prominent Cretaceous deformation history. If the latter is the case, Cretaceous fault reactivation can be regarded as a more widespread event than previously anticipated (e.g. Glorie and De Grave, 2016). With the use of the newly collected data from the Junggar Alatau, integrated with the published data, a more complete picture of the reactivation history of the Junggar Alatau in response to distal tectonic events at the Mesozoic southern Eurasian plate margin can be created. Furthermore, understanding whether the region records thermochronological evidence for Cenozoic deformation or preserves Mesozoic deformation is key to understanding the propagation of strain through crustal architecture of Central Asia.

Thermochronological data are presented for twenty-five samples, sixteen from SE Kazakhstan and nine from NW China, that were analysed by the AFT and apatite U–Pb (AU–Pb) methods. For two of these samples, supplementary apatite (U–Th)/He age data were obtained. Resulting thermal history models were produced to constrain the cooling history of the Junggar Alatau and to identify the timing of fault reactivation across its structural architecture.

2. Geological background and setting

The Junggar Alatau is primarily composed of Palaeozoic granitic plutons and Precambrian to Palaeozoic strata (e.g. Korobkin and Buslov, 2011; Petrov et al., 2016; Kröner et al., 2017; Han and Zhao, 2018; Li et al., 2018), forming the southwestern boundary of the Junggar Basin. The main exposed rock types range between granitoids, ophiolites, metamorphosed units and glacial to alluvial strata (e.g. Zhao and He, 2013; Huang et al., 2017; Li et al., 2018; Zhu et al., 2018). The Junggar Alatau forms a northern extension of the boundary between the Chinese North Tian Shan and the Yili-Central Tian Shan (e.g. Wang et al., 2018a,b), as part of the Central Asian Orgonic Belt (CAOB), and therefore, its geological history is strongly linked to that of the CAOB.

Accretion in the CAOB began at ca. 1000 Ma and its eventual amalgamation was completed at ca. 250 Ma, following the closure of the Palaeo-Asian Ocean (PAO) (e.g. Windley et al., 2007; Huang et al., 2017). Prominent Palaeozoic strike-slip structures formed and deformed during the amalgamation process (e.g. Laurent-Charvet et al., 2003; Li et al., 2017), which experienced episodic reactivation events after the closure of the PAO (e.g. Glorie et al., 2011, 2012a, 2019; Jepson et al., 2018a; Nachtergaele et al.,

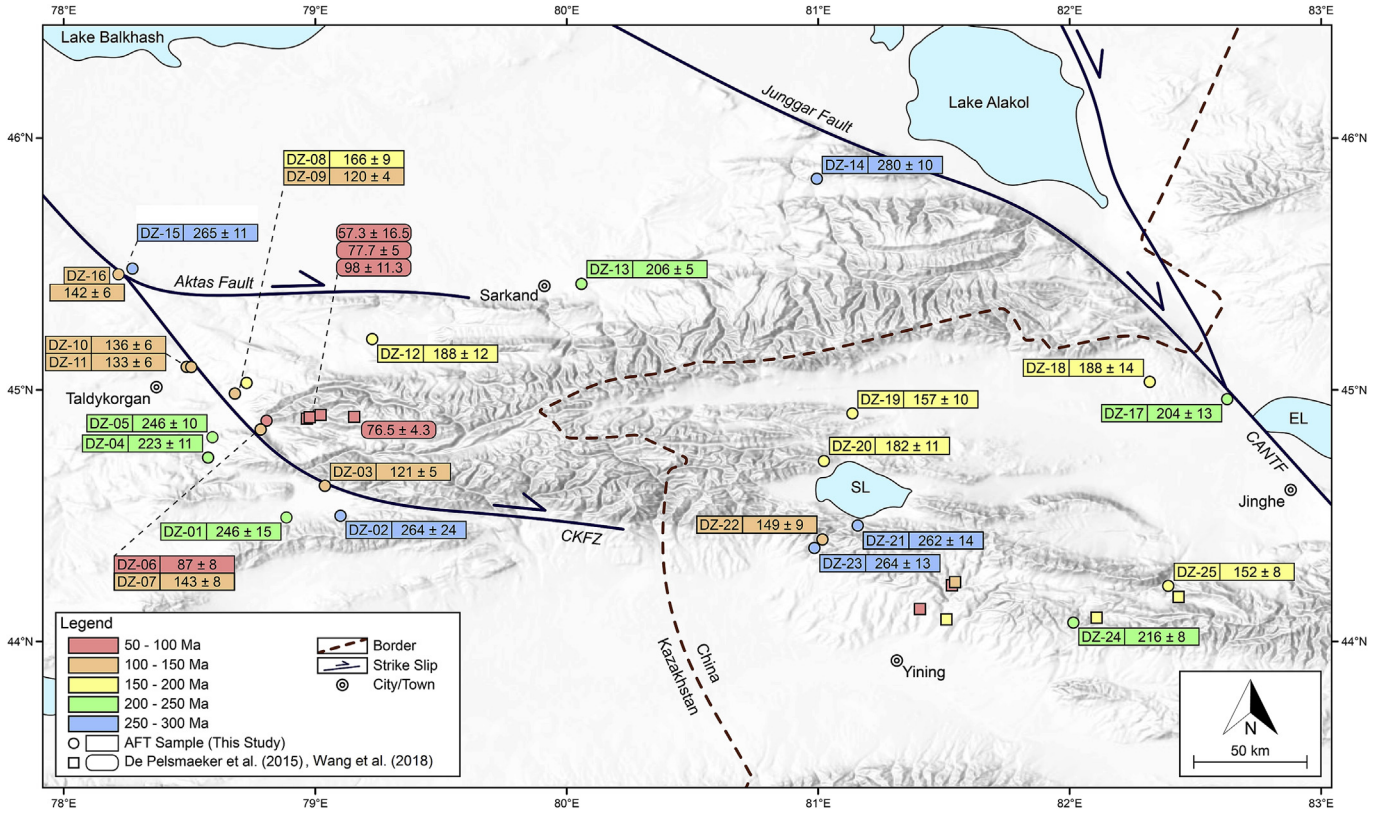

Fig. 2. Topographic map of the Junggar Alatau and surroundings. Dots indicate sample locations with AFT ages (in Ma) from this study and square symbols show the locations for previous results reported by De Pelsmaeker et al. (2015). AFT ages are colour coded at 50 Ma increments. The border shared by Kazakhstan and China is indicated by the dashed line. Strike slip faults are indicated by a solid line and an arrow indicating the direction of movement. Cities and towns are represented by ringed dots. Main faults after Choulet et al. (2012), De Pelsmaeker et al. (2015) and Li et al. (2018). CANTF = Chingiz-Alakol-North Tian Shan Fault, CKFZ = Central Kazakhstan Fault Zone, EL = Ebi Lake, SL = Sayram Lake.

2018). Structural and thermochronological data obtained for these strike-slip faults record evidence for both transpressional and transtensional reactivation in response to distant tectonic events (e.g. Glorie et al., 2012b; Li et al., 2017). Crustal shortening in response to distant Meso–Cenozoic tectonic events along the Eurasian margin is thought to be the main driver for the intra-continental deformation that shaped the mountain ranges that dominate the present-day Central Asian topography (De Grave et al., 2007; Jolivet et al., 2010; Choulet et al., 2013; De Pelsmaeker et al., 2015; Glorie and De Grave, 2016). The reactivation of these inherited Palaeozoic structures throughout the Meso–Cenozoic period has been attributed to the Cimmerian orogeny during the closure of the Palaeo-Tethys Ocean, the Mongol-Okhotsk orogeny during closure of the Mongol-Okhotsk Ocean, and the India-Eurasia collision during the closure of the Neo-Tethys Ocean (e.g. Glorie and De Grave, 2016). Punctuated accretion of Gondwana derived Cimmerian blocks led to the Cimmerian orogeny at the Mesozoic southern Eurasian margin. The Cimmerian terranes involved are the Qiangtang Block, which accreted during the Late Triassic–Early Jurassic, the Lhasa Block, which accreted during the latest Jurassic–Early Cretaceous, and the Karakoram Block and Kohistan-Dras island arc, which finalised the Cimmerian orogeny during the Late Cretaceous (e.g. De Grave et al., 2007; Glorie and De Grave, 2016).

In south-eastern Siberia, the diachronous oceanic closure between Mongolia-North China and Siberia resulted in the formation of the Mongol-Okhotsk Orogenic Belt (MOOB) (Jolivet et al., 2009). A 'scissor-like' closure model, supported by palaeomagnetic data, has been proposed by Metelkin et al. (2010) suggesting a W–E closure of the Mongol-Okhotsk Ocean during the Late Jurassic–Early Cretaceous due to the clockwise rotation of the Siberian craton (Metelkin et al., 2012).

A recent plate-tectonic reconstruction (Zahirovic et al., 2016) suggests that slab-rollback is thought to have initiated back-arc extension in the Tethys Ocean during the late Early Cretaceous, swiftly following the Lhasa and MOOB collisions. Although this period of extension has hitherto received little attention, it is likely that it may have caused fault-reactivation within Central Asia at that time. During the same time period, basins along southern Central Asia (e.g. the Fergana and Tarim basins) experienced marine incursions of the Para-Tethys Ocean (Bande et al., 2017; De Pelsmaeker et al., 2018; Jepson et al., 2018b), further suggesting that parts of Central Asia were subsiding during a period of intra-continental extension or transtension.

Following the Mesozoic reactivation events, India converged to the southern Eurasian margin resulting in the start of the Cenozoic India-Eurasia collision (e.g. Van Hinsbergen et al., 2012). Associated deformation is recorded in the thermal history of the southern CAOB, mostly during the late Oligocene-Miocene (e.g. Hendrix et al., 1994; Sobel and Dumitru, 1997; Bullen et al., 2001; Sobel et al., 2006a; Glorie et al., 2011; Macaulay et al., 2014; Jepson et al., 2018a).

Thermochronological results for the Junggar Alatau are scant. Few published AFT data by De Pelsmaeker et al. (2015) provide limited evidence for relatively fast cooling of the Junggar Alatau during the Cretaceous. These results were interpreted to be recording the collision of the Lhasa Block along the southern Eurasian margin, but the far-field effects of the MOOB were not discounted. Potential links with back-arc extension in the Tethys were not discussed. More recent AFT data in the vicinity of the

Junggar Alatau suggest a contrasting thermal history with significant early Mesozoic and Cenozoic cooling, while Cretaceous cooling was modelled to be rather slow (Wang et al., 2018b). Other AFT thermochronological studies at major NW–SE orientated shear zones, bisecting Central Asia, have mostly recorded Mesozoic thermal histories revealing rapid Triassic and Cretaceous cooling. Along the Irtysh and Talas-Fergana shear zones, located to the north and south of the Junggar Alatau respectively, studies by Glorie et al. (2012b) and Nachtergaele et al. (2018) reported Cretaceous AFT ages that were modelled to reflect fast cooling at that time. Results along the Irtysh shear zone were interpreted as a possible response to the far-field effects of the MOOB while results along the Talas-Fergana shear zone were interpreted as a response to the Lhasa collision.

Sedimentary records of surrounding basins record periodic deposition of sediments in response to deformation during the Meso-Cenozoic period. In this regard, the Junggar and Tarim basins record the deposition of conglomerates and coarse clastic alluvial sediments during the Late Triassic–Early Jurassic, Early Cretaceous, Late Cretaceous–Palaeocene, and Neogene (Hendrix et al., 1992; Dumitru et al., 2001; Jolivet et al., 2010; Choulet et al., 2013).

3. Methods

3.1. Laboratory processing

Samples were collected in the Junggar Alatau and prepared by crushing, sieving and mineral separation using standard methods at the Institute of Geology and Geophysics, Chinese Academy of Sciences (IGGCAS). At the University of Adelaide, the apatite grains were mounted in EpoxyCure resin onto thin section slides and then ground and polished to expose the grains. Etching of the samples was completed in a solution of 5 M HNO_3 for 20 ± 0.5 s at 20 ± 0.5 °C to reveal the natural fission tracks.

3.2. Apatite fission track analysis

Apatite fission track data record the thermal history of the samples through the apatite partial annealing zone (~60–120 °C) (Wagner et al., 1989). Imaging of individual grains from each sample was conducted on a Zeiss AXIO Imager M2m Autoscan System with a magnification of ×1000. Following imaging, fission track densities and confined track lengths in the individual grains were measured using FastTracks software. Measuring of ^{238}U concentrations in individual grains was conducted through 30 μm spot analysis using laser ablation inductively coupled plasma mass spectrometry (LA-ICP-MS) on a solid state New Wave-213 laser coupled with an Agilent 7900× mass spectrometer. Iolite software was used for the process of data reduction (Paton et al., 2011). NIST 610 was used as the primary standard and secondary standards of Durango and McClure apatite were both used to test the accuracy of the analysed data. More details on the applied methodology are to be found in Glorie et al. (2017b), Gillespie et al. (2017a) and Fernie et al. (2018). Instrumental settings are given in Supplementary File 1.

Durango apatite was used for zeta calibration (Vermeesch, 2017) of single-grain AFT ages for unknown apatite samples. The weighted average AFT age yielded by Durango apatite in this work was 30.1 ± 1.2 Ma (Supplementary File 2). This is value is within uncertainty of the published $^{40}Ar/^{39}Ar$ age of 31.44 ± 0.18 Ma (McDowell et al., 2005), suggesting reliable fission track results.

3.3. Apatite U–Pb analysis

Apatite uranium-lead (AU–Pb) dates record the timing of cooling between temperatures of ~350–550 °C (Chew et al., 2014; Chew and Spikings, 2015). In this work, the AU–Pb ages are mostly used as high-temperature references and compared against their respective AFT age to constrain whether the samples have experienced low-temperature (partial) resetting. Analytical procedures are identical to those in Glorie et al. (2017a ,b) and Gillespie et al. (2018). Instrumental settings are given in Supplementary File 1.

Durango and McClure apatites were used as accuracy checks for the U–Pb age of unknown apatite samples. Durango apatite yielded a ^{207}Pb corrected weighted average $^{206}Pb/^{238}U$ age of 32.22 ± 0.85 Ma and McClure apatite yielded an age of 529.4 ± 5.4 Ma (Supplementary File 3). These values are in good agreement to the published $^{40}Ar/^{39}Ar$ age for Durango apatite at 31.44 ± 0.18 Ma (McDowell et al., 2005) and the published AU–Pb age of McClure apatite at 524.6 ± 3.2 Ma (Chew et al., 2014). The AU–Pb age data for the analysed samples can thus be treated as being reliable.

3.4. Apatite (U–Th)/He analysis

Apatite (U–Th–Sm)/He (AHe) analysis dates the timing of cooling through temperatures of ~80–40 °C, making it a complementary technique to the fission track method (Ehlers and Farley, 2003). The AHe analyses for this study were undertaken at the John de Laeter Centre, Curtin University, and followed the protocols described in (Danisik et al., 2013). Apatite crystals were hand-picked, photographed and measured for physical dimensions, before being loaded in Pt microtubes. Helium (^4He) was extracted at ~900 °C, under ultra-high vacuum using a diode laser and measured by isotope dilution on a Pfeiffer Prisma QMS-200 mass spectrometer. A re-extract was run after each sample to verify complete outgassing of the crystals. Helium gas results were corrected for blank, determined by heating empty microtubes using the same procedure. After the ^4He measurements, tubes containing the crystals were retrieved from the laser cell, spiked with ^{235}U and ^{230}Th, and dissolved in HNO_3. Sample, blank, and spiked standard solutions were analysed by isotope dilution for ^{238}U and ^{232}Th and by external calibration for ^{147}Sm on an Element XR high-resolution ICP-MS. The raw AHe ages were corrected for alpha ejection (FT correction), whereby a homogenous distribution of U, Th, and Sm was assumed for the crystals. Replicate analyses of internal standard Durango apatite measured over the period of this study yielded mean AHe ages of 31.9 ± 1.0 Ma (1σ), consistent with the reference Durango AHe age of 31.02 ± 1.01 Ma (McDowell et al., 2005).

3.5. Low-temperature thermal history modelling

Using QTQt software version 5.6.0 (Gallagher, 2012), thermal history models were constructed using individual grain AFT data and additional AHe data, where available. Geological constraints (e.g. AU–Pb and depositional age) were added to resolve the thermal history. The temperature at the timing of deposition for the sedimentary samples has been set at 22.5 ± 2.5 °C. For basement samples, AU–Pb ages were introduced into the modelling, reflecting temperatures of 400 ± 50 °C. The modelling procedure involved running 10,000 possible models as a test run to gauge the plausibility of thermal history models. Models deemed as statistically acceptable were further refined by running an extra 200,000 possible models. QTQt software generates four different models: maximum likelihood, maximum posterior, maximum mode, and expected. In further discussion, the 'expected' models were used for each sample as these models returned the best match with the input data.

Table 1
Sample locations and lithology details. Crystallisation and depositional (indicated by asterisks) ages from Petrov et al. (2016).

Sample	Latitude (°N)	Longitude (°E)	Altitude (m)	Crystallisation/ Depositional ages*	Lithology
DZ-01	44.49281	78.89156	1440	Carboniferous	Granite
DZ-02	44.49974	79.10671	1776	Carboniferous	Granodiorite
DZ-03	44.61891	79.04423	1521	Carboniferous	Granodiorite
DZ-04	44.73114	78.57965	1011	Carboniferous	Granite
DZ-05	44.81153	78.59735	1038	Carboniferous	Granite
DZ-06	44.87727	78.81242	1114	Carboniferous	Granodiorite
DZ-07	44.84244	78.7892	1260	Carboniferous	Granite
DZ-08	45.02715	78.73286	1141	Carboniferous	Granodiorite
DZ-09	44.98546	78.68664	960	Carboniferous	Granodiorite
DZ-10	45.0916	78.49511	628	Carboniferous	Granitic Gneiss
DZ-11	45.09101	78.5129	648	Carboniferous	Granodiorite
DZ-12	45.20145	79.23236	1253	Permian	Granodiorite
DZ-13	45.42118	80.06469	1024	Permian	Granite
DZ-14	45.83873	81.00055	1042	Permian	Granodiorite
DZ-15	45.46473	78.25181	489	Permian	Granite
DZ-16	45.45921	78.22339	508	Permian	Granodiorite
DZ-17	44.96321	82.6329	208	Permian	Kspar Granite
DZ-18	45.03172	82.32456	668	Permian	Granite
DZ-19	44.90617	81.14242	1404	Silurian	Kspar Granite/ Leucogranite
DZ-20	44.7169	81.02879	2576	Carboniferous*	Fine Lithic Wacke
DZ-21	44.46077	81.1632	1856	Neoproterozoic*	Schist
DZ-22	44.40522	81.02278	1368	Carboniferous	Diorite
DZ-23	44.37169	80.99087	1228	Carboniferous	Altered Porphyritic Granite
DZ-24	44.07527	82.02129	1295	Permian	Kspar Granite
DZ-25	44.22109	82.39847	1453	Devonian	Granite

4. Results

4.1. Samples

A total of 25 samples were collected (Fig. 2, Table 1). All samples were analysed using the AFT method, 24 samples were analysed using the AU–Pb (one sample was excluded due to the relative absence of sufficient radiogenic Pb) and 2 by (U–Th)/He methods. Major NW–SE orientated shear zones were targeted to constrain the reactivation of the structural architecture. Twenty-three samples were sourced from Palaeozoic basement rocks of granitic to dioritic composition, in some cases showing alteration or gneissic metamorphism. DZ-20 was sourced from the Dongtujinhe Formation (~313–300 Ma; Huang et al., 2017) and DZ-21 from a metamorphosed sedimentary outcrop with an unknown age.

Samples are divided in three groups, based on their proximity to each other and to shear zones. Group 1 consists of eight samples (DZ-01, -02, -04, -05, -12, -13, -14 and DZ-15) that were taken distal to the CKFZ in the Kazakh part of the Junggar Alatau. Group 2 consists of eight samples (DZ-03, -06, -07, -08, -09, -10, -11 and DZ-16) that were taken in vicinity to the CKFZ. Group 3 consists of nine samples (DZ-17, -18, -19, -20, -21, -22, -23, -24 and DZ-25) that were taken from the Chinese part of the Junggar Alatau, predominantly distal to major shear zones (Fig. 2).

4.2. Apatite fission track (AFT) results

4.2.1. Group 1 samples (Kazakh samples, distal from the shear zone)

Group 1 is characterised by the oldest central AFT ages in the study region. Central AFT ages range from 280 ± 10 Ma to 188 ± 12 Ma (Fig. 2, Table 2, Supplementary File 4). All samples passed the χ^2 test and yield single-grain age dispersions of <25%,

Table 2
Summary AFT table organised by sample group. ρ_s represents the average density of spontaneous fission tracks in $10^5/cm^2$. N_s represents the number of tracks counted across all grains. n represents the number of grains analysed. ^{35}Cl and ^{238}U represent the average concentrations of the most abundant Chlorine and Uranium isotopes in ppm with 1σ as the reported uncertainty (anomalously high Cl concentrations for individual grains were excluded from the average calculations). t represents the central AFT age (in Ma), calculated with RadialPlotter (Vermeesch, 2009), with 1σ as the reported uncertainty. n_l represents the number of confined fission tracks measured in each sample. MTL represents the mean track length of the measured confined fission tracks with SD as the 1σ standard deviation of distribution (in μm). Disp represents the percentage of dispersion between single-grain AFT ages and P(χ^2) represents the probability that the analysed grains are of a single population (calculated with RadialPlotter).

Sample	ρ_s	N_s	n	^{35}Cl	1σ	^{238}U	1σ	t	1σ	n_l	MTL	SD	Disp	P(χ^2)
Group 1														
DZ-01	8.2	494	37	5213	1001	7.80	0.68	246	15	84	12.12	2.08	19	0.09
DZ-02	4.0	139	24	7061	1146	3.36	0.38	264	24	54	12.53	2.00	0	1.00
DZ-04	7.1	447	32	2046	691	7.13	0.50	223	11	45	11.11	1.93	0	0.68
DZ-05	10.7	1067	32	10253	1137	9.37	0.67	246	10	55	12.68	1.61	13	0.07
DZ-12	12.2	507	23	16677	3351	13.48	0.94	188	12	62	12.45	2.14	16	0.11
DZ-13	36.9	2799	43	2204	923	37.46	2.28	206	5	174	12.99	1.34	8.4	0.07
DZ-14	12.1	1510	40	11094	1535	8.95	0.61	280	10	100	13.60	1.26	12	0.05
DZ-15	5.7	801	36	531	201	4.81	0.30	265	11	94	12.95	1.60	9.9	0.12
Group 2														
DZ-03	9.9	1147	39	573	225	17.69	1.12	121	5	100	13.03	1.33	13	0.06
DZ-06	7.0	244	18	2901	584	17.83	1.20	87	8	38	11.28	1.83	22	0.06
DZ-07	12.7	534	27	3757	974	20.07	1.61	143	8	93	11.90	2.17	14	0.09
DZ-08	6.9	592	31	6277	599	9.36	0.86	166	9	72	12.79	1.80	16	0.11
DZ-09	15.7	1334	39	3214	863	28.08	1.83	120	4	100	12.58	1.83	10	0.06
DZ-10	5.0	884	40	4613	694	8.16	0.51	136	6	100	12.76	1.59	15	0.07
DZ-11	9.3	933	32	4774	911	14.03	1.15	133	6	80	12.69	1.54	15	0.05
DZ-16	10.8	1027	35	766	168	16.64	1.19	142	6	100	12.92	1.46	14	0.05
Group 3														
DZ-17	8.9	313	18	5609	1471	9.64	0.86	204	13	34	12.83	1.43	5.6	0.38
DZ-18	8.6	336	23	2998	815	9.53	0.76	188	14	100	12.04	1.60	19	0.13
DZ-19	6.8	268	25	1588	440	8.88	0.59	157	10	38	11.85	2.07	5	0.84
DZ-20	5.0	427	31	4095	776	6.16	0.43	182	11	82	13.33	1.59	15	0.33
DZ-21	9.5	588	31	9738	1476	8.07	0.54	262	14	82	12.09	1.89	17	0.06
DZ-22	7.3	438	29	4853	1094	10.79	0.78	149	9	79	12.10	1.74	17	0.07
DZ-23	12.6	714	31	10926	1259	10.06	0.81	264	13	100	12.69	1.71	14	0.08
DZ-24	12.7	1323	42	2026	389	12.82	0.89	216	8	100	11.91	1.73	14	0.05
DZ-25	18.6	817	27	8391	1454	28.13	2.26	152	8	100	12.36	1.61	16	0.07

suggesting each sample consists of a single-grain age population. Where sufficient number of confined fission tracks (benchmarked here and elsewhere at ≥80) were measured, mean track lengths (MTLs) vary between ~12.1 μm and ~13.6 μm (Table 2, Supplementary File 4). The pooled radial plot for Group 1 yields a central AFT age of 222 ± 4 Ma with a modest single-grain age dispersion of ~13% (Fig. 3).

4.2.2. Group 2 samples (Kazakh samples, in proximity to the shear zone)

Group 2 is characterised by the youngest central AFT ages in the study region. Central AFT ages range from 166 ± 9 Ma to 87 ± 8 Ma (Fig. 2, Table 2, Supplementary File 5). All samples passed the χ^2 test and yield single-grain age dispersions of <25%, suggesting each sample consists of a single-grain age population. Mean track lengths (MTLs) vary between ~11.9 μm and ~13.0 μm (Table 2, Supplementary File 5). The pooled radial plot for Group 2 yields a central AFT age of 121 ± 2 Ma with ~16% single-grain age dispersion. In general, high uranium concentrations are associated with the younger ages (~100 Ma) in the AFT age spectrum, and vice-versa (Fig. 3).

4.2.3. Group 3 samples (Chinese Junggar Alatau, mostly distal form shear zones)

The Central AFT ages for the Group 3 samples range from 264 ± 13 Ma to 149 ± 9 Ma (Fig. 2, Table 2, Supplementary File 6). All samples (including the sedimentary samples) passed the χ^2 test and yield single-grain age dispersions of <25%, suggesting each sample consists of a single-grain age population. Mean track lengths (MTLs) vary between ~11.9 μm and ~13.3 μm (Table 2, Supplementary File 6). The pooled radial plot for Group 3 yields a central AFT age of 183 ± 4 Ma with significant single-grain dispersion (~20%). The younger AFT ages (~150–100 Ma) are characterised by higher U concentrations (Fig. 3).

4.3. Apatite U–Pb results

Twenty-four samples yielded meaningful AU–Pb ages. Lower intercept ages range from the Late Ordovician (447 ± 20 Ma) to the early Permian (281 ± 25 Ma). AU–Pb ages are detailed in Table 3, where they are compared with the central AFT ages and (where available) with published zircon U–Pb (ZU–Pb) ages. Grains that experienced analytical problems (such as obvious down-hole zonation) were treated as outliers and were removed from the age calculations. AU–Pb Concordia plots can be found in Supplementary File 7.

4.4. Apatite (U–Th)/He results

Two samples (DZ-09 and DZ-16) from group 2 (near the CKFZ) yielded largely consistent Cretaceous AHe age data. Four grains of sample DZ-09 produced a mean AHe age of 102.8 ± 3.8 Ma with <2.5% 1σ reproducibility of the four individual dates. DZ-16 yielded a mean AHe age of 111.0 ± 3.4 Ma with ~8% 1σ reproducibility of the three individual dates (Table 4).

4.5. Thermal history modelling

Resulting 'expected' thermal history models are summarised in Fig. 4 and detailed in Supplementary File 8. Analysis of predicted versus observed modelling parameters can be found in Supplementary File 9.

4.5.1. Group 1 samples, distal to the shear zone

For Group 1, most samples record rapid cooling through the APAZ at ~290–270 Ma. While the models for DZ-14 and DZ-04 exit the APAZ in the Permian, other models (for DZ-01,-02,-05 and DZ-15) record subsequent prolonged residence at upper APAZ temperatures between ~270 Ma and ~110 Ma (Fig. 4). Note that the models for DZ-02 and DZ-05 are poorly constrained (limited confined length data) and, therefore, the apparent prolonged slow cooling phase should be interpreted with caution. More significant is the rapid cooling recorded by two additional samples (DZ-12 and DZ-13) at ~230–220 Ma. Sample DZ-04 records a modest re-entry into the APAZ during the Cretaceous, but this model is poorly constrained due to limited track length data.

In summary, the thermal history models for Group 1 record evidence for rapid cooling at ~290–270 Ma and at ~230–210 Ma.

4.5.2. Group 2 samples, proximal to the shear zone

Thermal history models for Group 2 (Fig. 4) record moderate to relatively rapid cooling through the APAZ between ~170 Ma and ~100 Ma (samples DZ-03, -09, -10, -11 and DZ-16). The models for samples DZ-09 and DZ-16 were calculated using a combination of independent AFT and AHe data and are, therefore, likely most reliable. These models record faster cooling through the APAZ at ~160–120 Ma, suggesting that the cooling rates for the other models may be underestimated. The models for DZ-07 and DZ-08

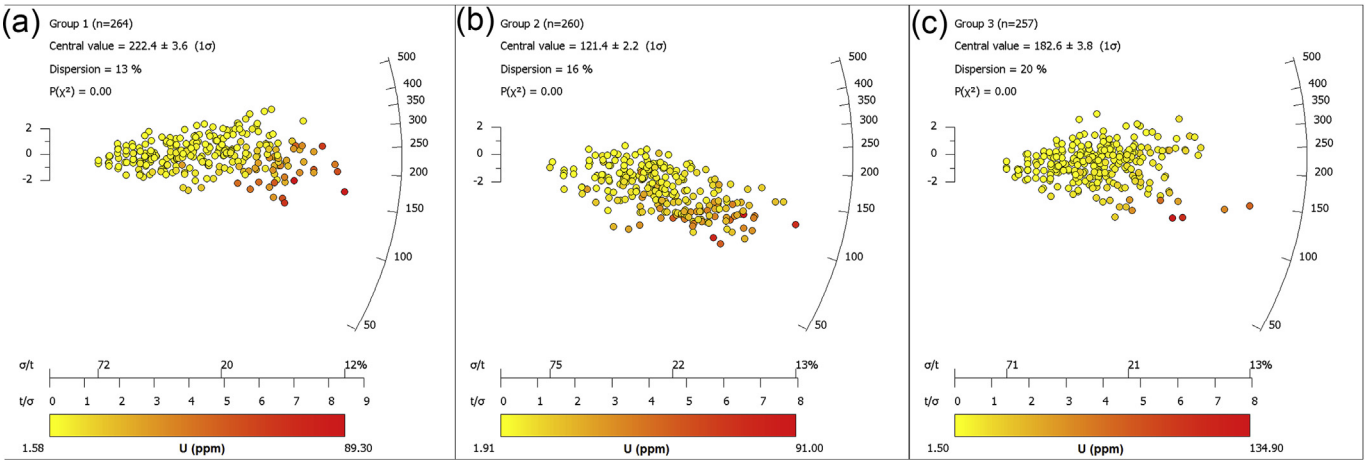

Fig. 3. Pooled AFT data plotted on radial plots for samples associated with Group 1 (a), Group 2 (b) and Group 3 (c). Radial plots and associated central age values and statistical parameters were calculated with RadialPlotter (Vermeesch, 2009). The coloured scale indicates the concentration of ^{238}U in ppm within the analysed grains.

Table 3
Summary AU–Pb age table, compared to AFT and ZU–Pb ages for each sample, organised by sample number. *n* represents the number of grains used in AU–Pb analysis. MSWD represents the mean square weighted deviation of AU–Pb data. AU–Pb Age is given by the lower intercept age of the Tera-Wasserburg Concordia plot with 95% confidence uncertainty. AFT age represents the central AFT age calculated with RadialPlotter (Vermeesch, 2009) with 1σ as the reported uncertainty. ZU–Pb age is the crystallisation/depositional age from published data reported by De Pelsmaeker et al. (2015), Huang et al. (2017), Wang et al. (2018a,b) and references therein. Samples with no published ZU–Pb data use mapped ages reported by Petrov et al. (2016) and are referred to by geologic age. Asterisks indicate the youngest zircon age from a detrital population.

Sample	Lithology	*n*	MSWD	AU–Pb age (Ma)	2σ (Ma)	AFT age (Ma)	1σ (Ma)	Published ZU–Pb ages (Ma)
DZ-01	Granite	25	1.7	335	21	246	15	~340
DZ-02	Granodiorite	-	-	-	-	264	24	~340
DZ-03	Granodiorite	43	1.6	379	14	121	5	~340
DZ-04	Granite	19	1.2	304	24	223	11	~340
DZ-05	Granite	28	1.5	397	24	246	10	~340
DZ-06	Granodiorite	19	1.5	310	13	87	8	~340
DZ-07	Granite	28	1.8	380	17	143	8	~340
DZ-08	Granodiorite	25	1.7	376	20	166	9	~340
DZ-09	Granodiorite	37	1.2	362	8	120	4	~340
DZ-10	Granitic Gneiss	34	0.7	434	20	136	6	Silurian
DZ-11	Granodiorite	34	1.5	410	30	133	6	Silurian
DZ-12	Granodiorite	19	1.4	280	29	188	12	298–260
DZ-13	Granite	36	1.4	283	10	206	5	298–260
DZ-14	Granodiorite	35	1.2	330	29	280	10	298–260
DZ-15	Granite	36	0.7	431	58	265	11	Silurian
DZ-16	Granodiorite	33	1.2	290	11	142	6	298–260
DZ-17	Kspar Granite	15	0.8	297	18	204	13	306–292
DZ-18	Granite	20	1.1	281	25	188	14	306–292
DZ-19	Kspar Granite	15	1.7	414	23	157	10	Silurian
DZ-20	Fine Lithic Wacke	32	1.5	353	13	182	11	~313*
DZ-21	Schist	29	0.9	447	20	262	14	Neoproterozoic
DZ-22	Diorite	28	1.3	373	13	149	9	Carboniferous
DZ-23	Porphyritic Granite	34	1.1	387	14	264	13	Carboniferous
DZ-24	Kspar Granite	43	1.2	351	6	216	8	Permian
DZ-25	Granite	22	1.5	391	10	152	8	Devonian

Table 4
Apatite (U–Th)/He results, including those obtained for the Durango standard. Concentrations of thorium, uranium and samarium are in ng. He is the concentration of helium measured in ncc. TAU is the total analytical uncertainty. Th/U is the ratio of thorium to uranium. eU is the effective uranium. Raw age is the age before the FT correction. FT is the alpha-ejection correction parameter based on the effective spherical (ES) radius of each crystal. Cor. age is the age after applying the FT correction.

Sample	^{232}Th	±		^{238}U	±		^{147}Sm	±		He	±	TAU	Th/U	eU	Raw age	±1σ	Ft	±	ES radius	Cor. age	±1σ
	(ng)	(%)	(ppm)	(ng)	(%)	(ppm)	(ng)	(%)	(ppm)	(ncc)	(%)	(%)		(ppm)	(Ma)	(Ma)		(%)	μm	(Ma)	(Ma)
DZ09-1	0.095	5.8	48.9	0.049	6.0	25.4	1.852	1.0	953.5	0.680	1.2	3.9	1.91	36.89	64.1	2.5	0.61	5	40	**105.2**	**6.7**
DZ09-2	0.035	4.1	8.5	0.041	4.3	9.9	1.552	0.7	373.8	0.567	1.0	3.1	0.85	11.88	74.7	2.3	0.73	5	57	**101.9**	**6.0**
DZ09-3	0.038	5.9	19.7	0.040	5.9	21.0	1.087	0.9	569.5	0.478	0.9	4.3	0.93	25.66	67.6	2.9	0.65	5	43	**104.3**	**6.9**
DZ09-4	0.020	4.3	15.2	0.021	4.5	15.9	0.776	1.0	596.5	0.220	1.2	3.2	0.95	19.46	57.0	1.8	0.57	10	36	**99.6**	**10.5**
																			Mean age	**102.8**	**3.8**
DZ16-2	0.109	4.1	53.2	0.063	4.3	30.9	1.551	0.5	758.4	0.810	1.0	3.1	1.71	43.39	65.4	2.0	0.61	5	40	**107.1**	**6.3**
DZ16-3	0.111	5.8	53.6	0.061	5.9	29.6	1.497	0.8	722.7	0.822	1.0	4.1	1.80	42.18	67.5	2.7	0.64	5	44	**104.7**	**6.7**
DZ16-4	0.117	4.1	46.3	0.075	4.3	29.8	1.548	0.9	612.0	1.152	1.0	3.1	1.54	40.73	81.4	2.5	0.67	5	47	**121.2**	**7.1**
																			Mean age	**111.0**	**3.4**
Durango-1	1.441	4.1		0.091	4.3		2.427	0.5		1.718	1.2	3.4	15.80		31.3	1.1	1.00	5		**31.3**	**1.9**
Durango-2	1.801	5.8		0.109	5.9		2.583	0.7		2.176	0.9	4.7	16.40		32.2	1.5	1.00	5		**32.2**	**2.2**
Durango-3	0.979	4.1		0.053	4.3		1.993	0.9		1.182	0.9	3.4	18.22		32.3	1.1	1.00	5		**32.3**	**1.9**
Durango-4	1.064	5.8		0.052	5.9		1.721	0.8		1.227	0.9	4.8	20.33		31.8	1.5	1.00	5		**31.8**	**2.2**
																			Mean age	**31.9**	**1.0**

(poorly constrained) record earlier entrance into the APAZ at ~200–180 Ma, followed by slow cooling throughout the Cretaceous. The poorly constrained model for sample DZ-06 enters the APAZ later, at ~120 Ma, and suggests a second cooling phase at ~30 Ma. However, given that the model is rather poorly constrained by limited confined length data, we do not interpret this cooling phase in further discussion.

In summary, the thermal history models for Group 2 record evidence for rapid cooling through the APAZ at ~160–120 Ma.

4.5.3. Group 3 samples, Chinese Junggar Alatau

Thermal history models for Group 3 (Fig. 4) preserve evidence for Palaeozoic cooling through the APAZ (~310–260 Ma; samples DZ-23 and DZ-24). The model for sample DZ-23 records subsequent slow cooling to present-day ambient conditions, while the model for DZ-24 resides at upper APAZ temperatures until the start of the Cenozoic. The models for two other samples (DZ-17 and DZ-18) suggest a rapid cooling event at ~220–200 Ma. The models for samples DZ-19, DZ-22 and DZ-25 record slower cooling rates, residing at APAZ temperatures during most of the Mesozoic. Two sedimentary samples were modelled, constrained to surface temperatures at the timing of deposition. The model for sample DZ-20 was constrained using the depositional age of the Dongtujinhe Formation, which is interpreted to range of ca. 313–300 Ma (Huang et al., 2017). The thermal history model indicates heating throughout the late Palaeozoic to reach a maximum temperature approaching ~120 °C during the middle Triassic. Subsequent cooling since the late Triassic was relatively slow, mimicking the cooling paths of samples DZ-19, DZ-22 and DZ-25. Sample DZ-21 was not modelled as its depositional age is uncertain.

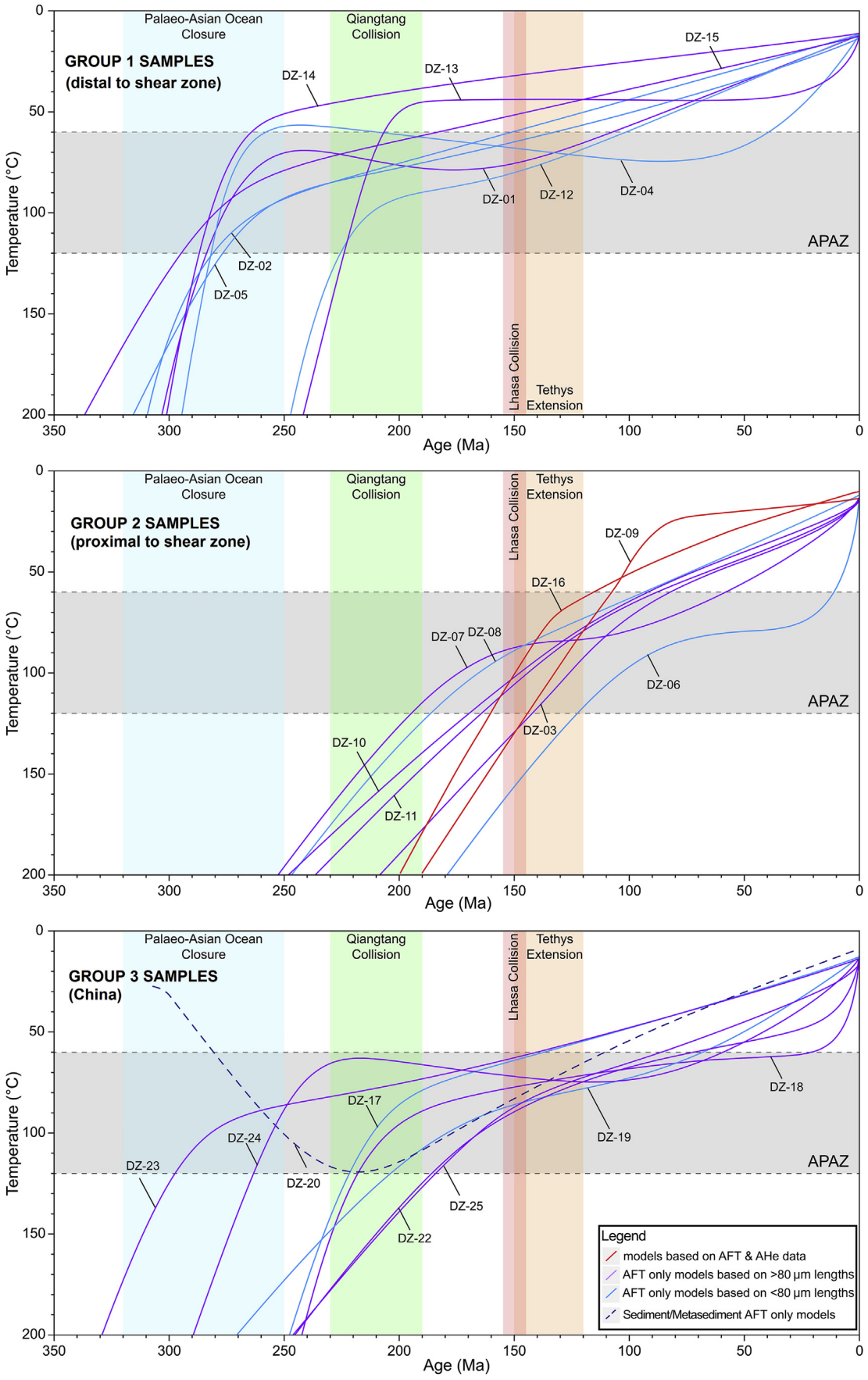
GROUP 1 SAMPLES
(distal to shear zone)
Palaeo-Asian Ocean Closure
Qiangtang Collision
Lhasa Collision
Tethys Extension
APAZ
DZ-15
DZ-14
DZ-13
DZ-01
DZ-12
DZ-04
DZ-02
DZ-05
Temperature (°C)
Age (Ma)
GROUP 2 SAMPLES
(proximal to shear zone)
DZ-09
DZ-16
DZ-07
DZ-08
DZ-06
DZ-03
DZ-10
DZ-11
GROUP 3 SAMPLES
(China)
DZ-17
DZ-18
DZ-24
DZ-19
DZ-23
DZ-20
DZ-25
DZ-22
Legend
models based on AFT & AHe data
AFT only models based on >80 µm lengths
AFT only models based on <80 µm lengths
Sediment/Metasediment AFT only models

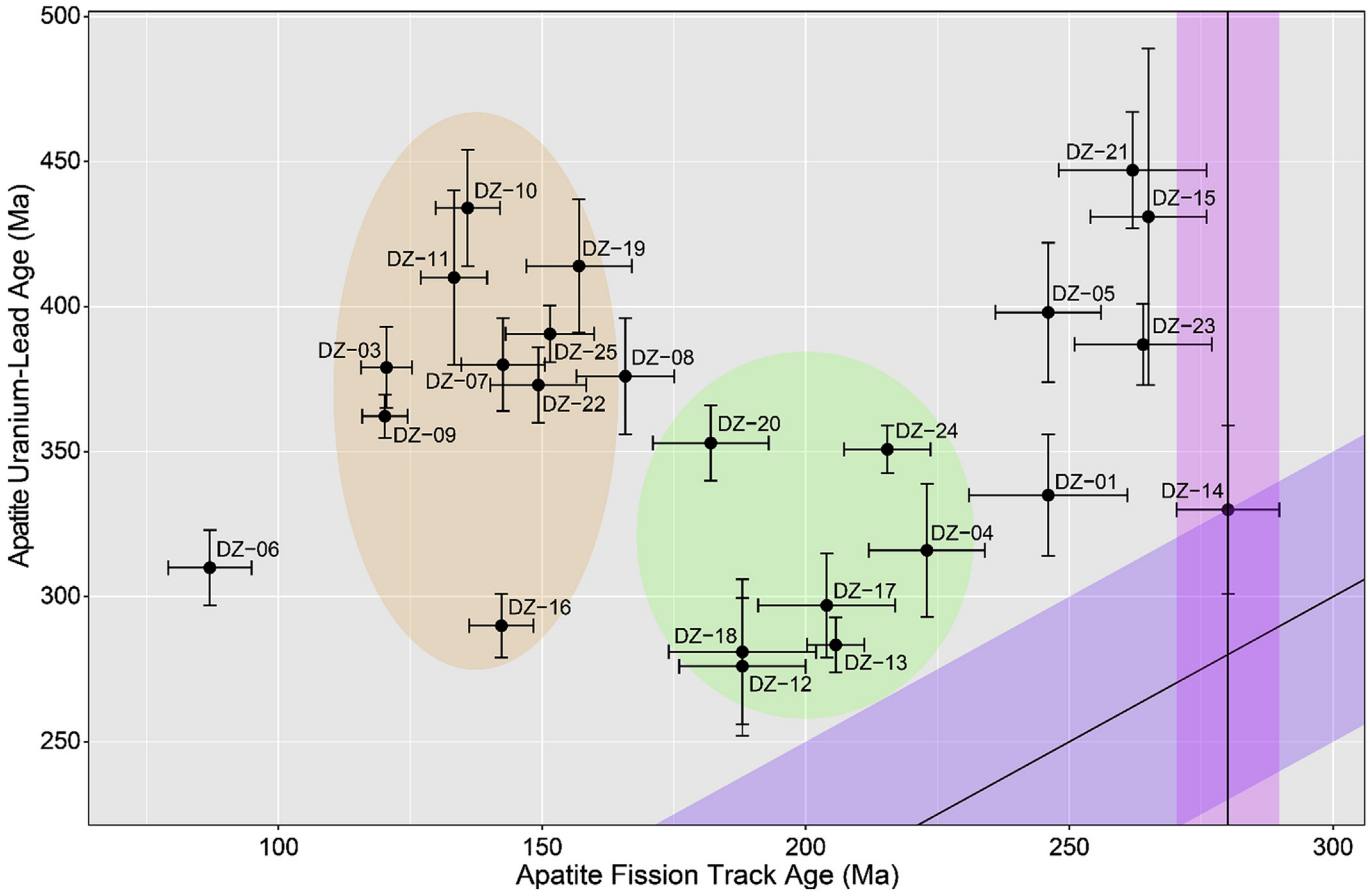

Fig. 5. AU–Pb vs AFT plot of all samples excluding DZ-02 (no AU–Pb age was obtained for this sample). Error bars for each sample represent the uncertainty of the AU–Pb age in Ma on the y-axis and AFT age in Ma on the x-axis. The pink band is the youngest AU–Pb age ± uncertainty and the purple band represents a 1:1 age relationship between AU–Pb and AFT ages. Samples outside these two bands record post-magmatic (partial) thermal resetting. Samples in the green and orange zones record thermal resetting at a time period that corresponds with major tectonic events at the distant plate margins (see text).

In summary, the thermal history models for Group 3 record rapid cooling at ~310–260 Ma and at ~220–220 Ma. The sedimentary sample records maximum temperatures (~120 °C) in the middle Triassic.

5. Interpretations and discussion

5.1. Apatite U–Pb (AU–Pb) age interpretations

The AU–Pb dates are compared to published (zircon U–Pb) crystallization ages (Table 3) (De Pelsmaeker et al., 2015; Petrov et al., 2016; Huang et al., 2017; Wang et al., 2018a) to identify which AU–Pb dates can be attributed to crystallization ages (i.e. when AU–Pb ages are within uncertainty to the published crystallization ages). However, for most of the analysed samples, precise zircon U–Pb dates are lacking and age ranges were obtained from geological maps. The AU–Pb dates for samples DZ-01, -04, -06, -10, -11, -12, -13, -15, -16, -17, -18, -19 and DZ-25 are within uncertainty the same to the reported crystallization ages. The AU–Pb dates for the other samples (DZ-03, -05, -07, -08, -09, -11, -14, -20, -22, -23 and DZ-24) are significantly (up to ~50 Ma) older than the reported ZU–Pb or mapped ages. This age discrepancy is likely a result of poor crystallisation age constraints, and therefore, the AU-Pb dates can be used to refine the crystallization ages of the sampled intrusions. Sample DZ-21 was taken from a Neoproterozoic schist, producing a reasonably well-constrained AU–Pb date of 447 ± 20 Ma. It is unclear if this age represents the timing of deposition (in conflict with the mapped Neoproterozoic age) or rather a metamorphic overprint. Here, the AU–Pb dates are used as a high-temperature constraint and further details on their relevance in terms of crystallization/deposition beyond the scope of this work.

5.2. AFT age interpretations and comparison with AU–Pb age constraints

The thermal history models across the Junggar Alatau display different thermal histories, preserving fast cooling signals during

Fig. 4. Summary thermal history models, based on expected tT outputs from QTQt in Supplementary File 8. Models based on both AFT and AHe data are displayed in red, those that have AFT only and that are based on at least 80 μm confined AFT lengths are displayed in purple. Blue models are poorly constrained and should be interpreted with caution. These are based on AFT data only with less than 80 μm confined lengths. The dashed model is for a sedimentary sample. More details can be found in the text and Supplementary Files 8 and 9. Group 1 and Group 3 samples show a dominant cooling signal during the late Palaeozoic, interpreted to be related with exhumation and post-magmatic cooling after granitoid crystallization in the framework of the closure of the Palaeo-Asian Ocean. Few models record fast cooling during the Triassic, which can be correlated with the Qiangtang collision. Group 2 samples reveal a consistent pattern of significant cooling during the Cretaceous, contemporaneous with the distant Lhasa collision and subsequent extension in the Tethys Ocean.

(1) the late Carboniferous–early Permian, (2) the Late Triassic and (3) the Late Jurassic–Early Cretaceous (Fig. 4). In order to interpret these cooling events, firstly the AU–Pb and AFT dates are compared per sample. Such comparison is particularly relevant to interpret the driver for the late Carboniferous–early Permian cooling signal. Fig. 5 plots the AFT versus AU–Pb ages, with the pink band representing the youngest AU–Pb age ± uncertainty, recorded for the study area (interpreted as the youngest granitoid crystallization phase), while the purple band represents a 1:1 age relationship between the AU–Pb and AFT ages with a maximum 2σ uncertainty. Therefore, samples outside of the pink and purple bands display evidence for (partial) thermal resetting after crystallization.

DZ-14 records the oldest AFT age, which is equivalent (within uncertainty) to the youngest AU–Pb age for the study area (i.e. DZ-14 plots in the pink band of Fig. 5). Hence, this sample cooled rather quickly after crystallization and has not experienced any significant subsequent thermal event. Similarly, the uncertainties on the AFT ages for samples DZ-15 and DZ-23 are within the uncertainty range of the pink band in Fig. 5, suggesting that these samples have not experienced significant thermal events after crystallization. All other samples lie outside the pink and purple bands, indicating that they have experienced prolonged cooling or thermal resetting after crystallization. The highlighted zones coloured green and orange in Fig. 5 correspond to the timing of two different thermo-tectonic events that affected the southern Eurasian margin during the Late Triassic–Early Jurassic and Cretaceous, discussed below.

The relative distance of the sample symbols in Fig. 5 with respect to the pink and purple bands may provide some insights into which samples likely record post-magmatic cooling and exhumation versus more significant thermal events. In this regard, the notable proximity of the sample symbols with AFT ages >180 Ma (except DZ-20 and DZ-24) to either pink or purple bands, and the apparent trend in the data that follows the pink and purple bands, may suggest that the AFT ages for those samples could be attributed to post-magmatic cooling. However, at least some samples deviate from this main trend (DZ-20 and DZ-24) and given that the age difference between AU–Pb and AFT ages generally exceeds 60 Ma, it is more likely that the Triassic and early Jurassic cooling ages (green area in Fig. 5) at least partially record evidence for a different thermal event at that time. For all samples with AFT ages <180 Ma (orange area in Fig. 5), it is clear that there is no relation with the AU–Pb dates, suggesting a prominent post-magmatic thermal event during the Cretaceous.

5.3. Boomerang plot

The 'boomerang' plot displays the relationships between the AFT age and Mean Track Length (MTL) for each sample (Green, 1986; Gallagher et al., 1998), which can be used to identify the timing of thermal events from apparent AFT data. In this plot, each 'blade' of a 'boomerang trend' identifies a period of rapid cooling (long MTLs), while the central part of the boomerang trend reveals

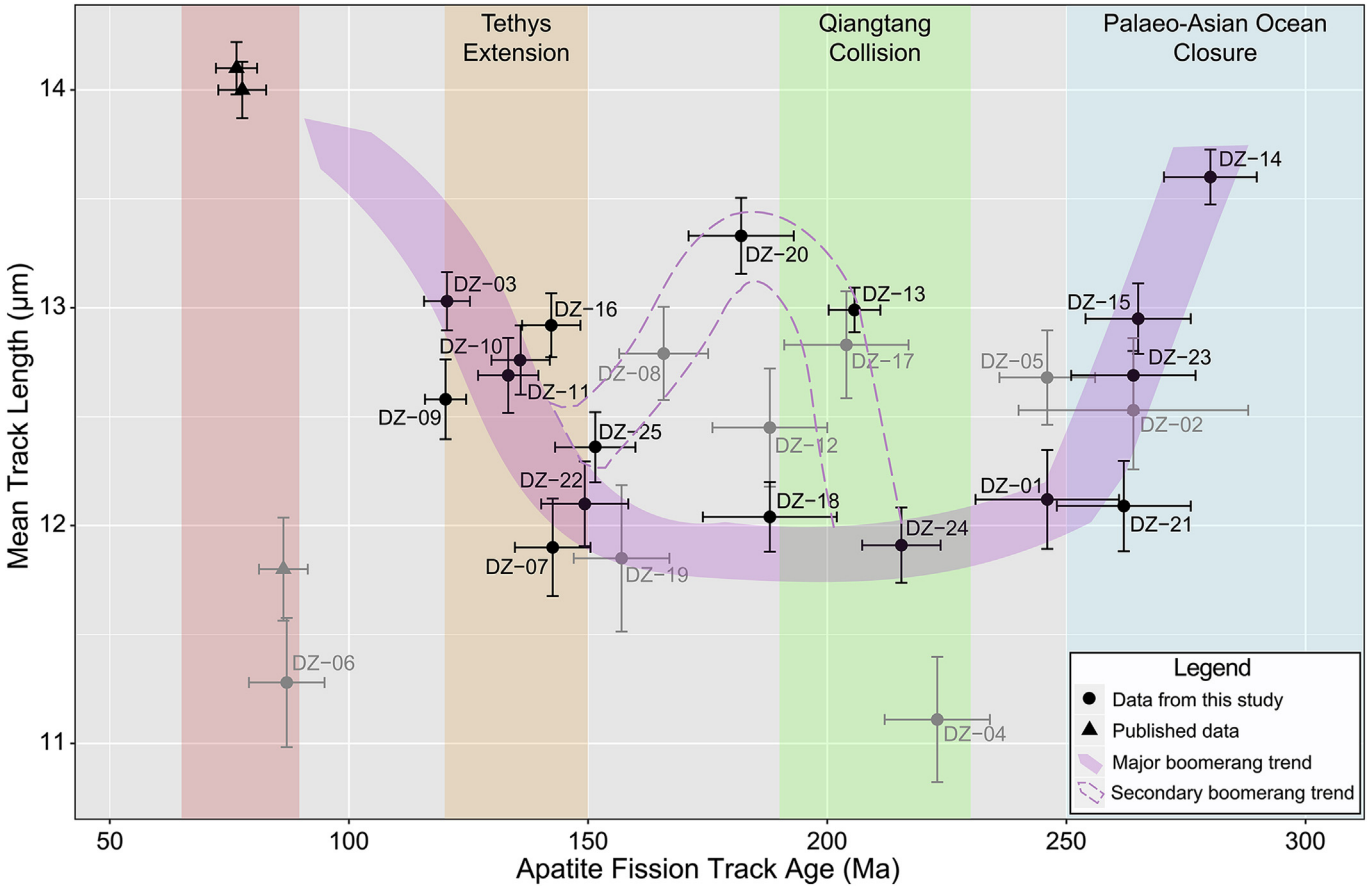

Fig. 6. 'Boomerang plot' based on the relationship between MTL and AFT ages. Samples from this study are indicated by circles and triangle symbols show previous results reported by De Pelsmaeker et al. (2015). Samples with less than 80 µm confined tracks are displayed as gray symbols and should be treated with caution when evaluating patterns in the data. Error bars represent the uncertainty of the MTL in µm on the y-axis and AFT age in Ma on the x-axis. Blue zone = Palaeo-Asian Ocean closure, green zone = Qiangtang collision, orange zone = Tethys extension, and red zone = Late Cretaceous thermo-tectonic event. The arrows indicate the main trends through the data, suggesting several 'boomerang' patterns (refer to text for more details).

the timing of slow cooling (mostly short MTLs, reflecting prolonged APAZ residence).

The samples of this study along with samples analysed by De Pelsmaeker et al. (2015) reveal patterns that can be associated with at least one, possibly two, different boomerang trends throughout the late Palaeozoic–Mesozoic (Fig. 6). Initially, rapid cooling is recorded in the early Permian (~280 Ma), representing the youngest phase of magmatic crystallization (Figs. 5 and 6). This event is followed by slow cooling and APAZ residence, indicated by increasingly shorter MTLs during the Late Permian–Middle Triassic (~260–225 Ma). From the Late Triassic–Early Jurassic (~225–180 Ma), the MTLs gently increase in value, suggesting more rapid cooling rates. This defines a second 'boomerang blade', suggesting rapid cooling coinciding with the timing of the Qiangtang collision (e.g. Glorie and De Grave, 2016). The Middle to Late Jurassic (~170–150 Ma) is characterised by decreasing MTLs, defining a period of slow cooling and increased APAZ residence, which is followed by a new, more significant 'boomerang blade' (increase in MTLs) at ~150–120 Ma. This trend suggests rapid cooling during the Early Cretaceous, post-dating the Lhasa collision and coinciding with a period of back-arc extension in the Tethys Ocean (e.g. Zahirovic et al., 2016). Published AFT data (De Pelsmaeker et al., 2015), in combination with the AFT data for sample DZ-06, suggests a new phase of rapid cooling at ~80–70 Ma. It is, however, important to note that the data that define the apparent Triassic and late Cretaceous boomerang blades are rather scattered and mostly poorly constrained (gray symbols in Fig. 6, based on <80 μm confined track length measurements). Therefore, the apparent Triassic and late Cretaceous phases of increased cooling rates should be treated with caution and are clearly secondary to the main boomerang trend, defined by late Palaeozoic post-magmatic cooling and exhumation, and a subsequent early Cretaceous cooling phase. Hence, the combined information from Figs. 5 and 6 suggests that the significant Early Cretaceous cooling phase reflects a prominent thermo-tectonic event, while only little evidence was found for thermal responses to the Qiangtang collision in the study area.

5.4. Geographical distribution of cooling events and cooling mechanism

Different thermal histories are preserved in the study area as indicated above. Geographical differences across the Junggar Alatau can be used to associate preserved cooling signals with the structural architecture of the study area. Samples in Groups 1 and 3, which are distal to the CKFZ (Fig. 2), primarily preserve either (1) post-magmatic cooling ages for intrusions that were emplaced during the progressive closure of the PAO (e.g. Huang et al., 2017; Windley et al., 2007) or (2) cooling ages related to exhumation during the Qiangtang collision with Eurasia (e.g. Jolivet et al., 2010; Choulet et al., 2013). In contrast, samples in Group 2 (in proximity to the CKFZ) record the prominent Early Cretaceous rapid cooling phase, suggesting that the CKFZ was reactivated during the Early Cretaceous. Furthermore, the cooling histories at either side of the CKFZ are remarkably different, suggesting a local, fault-related, differential exhumation as the mechanism for the differential cooling. This can be illustrated by samples DZ-15 and DZ-16, which were taken in close vicinity to each other, on opposite sides of the shear zone, recording vastly different cooling histories and AFT ages of 265 ± 11 Ma and 142 ± 6 Ma, respectively (Figs. 2 and 4). There is no notable chemical difference recorded for the apatites in each sample (such as Cl concentration) that could influence the annealing rate, suggesting that DZ-16 records the fault reactivation during the Early Cretaceous while DZ-15 preserves an older thermo-tectonic event, indicating that the eastern side of the shear zone was tectonically stable at that time.

The mechanism of the Early Cretaceous cooling phase can be attributed to (1) the collision of Lhasa with Eurasia (e.g. Dumitru et al., 2001; Brunet et al., 2017), (2) extension in the Tethys Ocean (Zahirovic et al., 2016) or (3) the Mongol-Okhotsk Orogeny (e.g. Jolivet et al., 2009; Metelkin et al., 2012), as all these events can be correlated in time to the recorded rapid Early Cretaceous cooling phase. A compressional regime would require denudation after uplift to reset the fission track clock, inducing a significant time lag between uplift and AFT reset (Glorie and De Grave, 2016). In contrast, an extensional/transtensional regime would rapidly reset the AFT ages in close vicinity to the fault. In the latter stress regime, rapid footwall exhumation occurs with respect to a rapidly subsiding hanging wall (Stockli et al., 2000; Stockli, 2005).

Hence, this work suggests that the CKFZ was reactivated in a transtensional or extensional stress regime during the Early Cretaceous, recording a distal response to extensional tectonics in the Tethys Ocean at that time. This interpretation is in agreement with Jolivet et al. (2001), where reported AFT cooling ages along the Altyn-Tagh fault (a major structure in Central Asia in closer vicinity to the Lhasa terrane than the study area for this work) cannot be correlated with the Lhasa collision, suggesting that the Lhasa collision did not induce significant cooling and fault reactivation into (northern) Central Asia. The influence of the Mongol-Okhotsk Orogenic Belt (MOOB) is perhaps more ambiguous. Jolivet et al. (2007) found that the summits of the Gobi Altai, to the east of the Tian Shan and more proximal to the MOOB, preserves Jurassic relief. More recently, McDannell et al. (2018) confirmed the presence of old topography in Mongolia, but suggested that most of the central Mongolian relief developed during the Cretaceous in response to collision in the MOOB. Hence, although we cannot fully rule out that the Junggar Alatau may have been affected by a far-field response to the MOOB collision, the abrupt step in cooling ages across the CKFZ contrasts with the gradual, broad-scale cooling age variations across the Hangay dome (McDannell et al., 2018).

5.5. Interpretation and discussion of the thermo-tectonic history of the Junggar Alatau

5.5.1. Early Permian–Early Triassic

The Early Permian–Early Triassic AU–Pb and AFT ages are interpreted in relation to granitoid emplacement, post-magmatic cooling and subsequent exhumation in response to the closure of the PAO. Similar published AFT ages for the Tian Shan and neighbouring regions are limited, likely as a result of deformation overprint in response to more recent thermo-tectonic events. Dumitru et al. (2001) reported latest Palaeozoic AFT ages at Aksu and along the Dushanzi-Kuqa highway in the Tian Shan, while Song et al. (2018) found similar AFT data in the southwestern Alxa Tectonic Belt. Alternatively, cooling after regional heating associated with the Permian Tarim mantle plume was suggested as a reason for the rapid cooling of emplaced granitoids (Song et al., 2018). After the closure of the PAO, tectonic quiescence is recorded, indicated by shortening MTLs (Fig. 6) until ~225 Ma.

5.5.2. Late Triassic–Early Jurassic reactivation

Late Triassic–Early Jurassic rapid cooling is recorded by few samples in the study area. Although it's relevance can be debated (see above), this cooling event is here interpreted to be a (partially preserved) record of the accretion of the Qiangtang Block along the southern Eurasian margin (Glorie and De Grave, 2016). Similar AFT cooling ages were obtained for preserved old relief to the southwest of our study area, in the Kyrgyz Tian Shan (e.g. De Grave et al., 2011) and western Tian Shan (e.g. Jepson et al., 2018c). Upper Triassic–Lower Jurassic conglomerate sediments were observed in both the Junggar and Tarim basins, indicating that the region

underwent significant erosion following exhumation at that time (Hendrix et al., 1992; Dumitru et al., 2001; Jolivet et al., 2010; Choulet et al., 2013). In addition, conglomerate units occur within coal-bearing basins of Kazakhstan, further suggesting that a significant relief was denudating in Kazakhstan during the Triassic–Jurassic transition (Buvalkin, 1978).

Following the collision of the Qiangtang Block, an extensive peneplanation surface developed during the Middle to Late Jurassic period, suggesting a period of relative tectonic quiescence (Hendrix et al., 1992; Dumitru et al., 2001; Jolivet et al., 2010). The flat cooling paths during the Jurassic (Fig. 4), and short MTLs for Jurassic AFT ages (Fig. 6), fit well with this period of no tectonic activity.

5.5.3. Cretaceous reactivation

The Early Cretaceous rapid cooling event is evidenced in the thermal history models of Group 2 (samples in close vicinity to the CKFZ) (Fig. 4). Associated deposition of Lower Cretaceous conglomerates in the Junggar and Tarim basins (Hendrix et al., 1992; Dumitru et al., 2001; Jolivet et al., 2010; Novikov, 2013), supports that rapid cooling can be linked to a period of exhumation at that time. As discussed above, we interpret the rapid, localized exhumation as a response to reactivation of the CKFZ, in an extensional/transtensional regime.

AFT studies focussed on similar, major NW–SE orientated shear zones within Central Asia (Glorie et al., 2012b; Jepson et al., 2018c; Nachtergaele et al., 2018) report similar rapid cooling histories for the Early or early Late Cretaceous. While such cooling signals have previously, rather arbitrarily, been interpreted as a response to the Lhasa collision or even the MOOB collision (e.g. Glorie and De Grave, 2016 and references therein), there is a growing number of studies where the localised rapid cooling signals within are attributed to extension or transtension in response to slab-rollback of the subducting Tethys Ocean (Zahirovic et al., 2016). Petrological evidence for lithosphere–asthenosphere interaction in relation to slab roll-back in the Tethys since ~100 Ma can be found in present-day southern Tibet (Ma et al., 2013). This work thus favours a similar interpretation for the localised Cretaceous cooling signals found along the CKFZ, suggesting that the NW–SE crustal architecture of Central Asia had a profound control on exhumation at that time. In our interpretation, the Cretaceous relief and tectonic setting of the western CAOB may have been similar to the present-day Basin-and-Range Province in the western USA.

De Pelsmaeker et al. (2015) interpreted Late Cretaceous AFT ages within the Junggar Alatau to be related with the Lhasa or MOOB collision, suggesting a significant time-lag (~50–100 Myr) between exhumation and the collision. However, as discussed above, the localised nature of the Early Cretaceous AFT data near the CKFZ favours a model of extension or transtension at that time. Hence it is unlikely that Late Cretaceous cooling is related to an event that occurred prior to Tethys extension, which is not recorded in the shear zone. In fact, it has been suggested that the Zaisan Basin (eastern Kazakhstan) formed during the Late Cretaceous (Martinson et al., 1983; Venus et al., 1980; Blackbourn, 2015), which would support a period of extension/transtension at that time. More generally, AFT samples across the Kyrgyz Tian Shan (e.g. De Grave et al., 2013; Glorie and De Grave, 2016) and Chinese Tian Shan (e.g. Jia et al., 2015; Wang et al., 2009) record Late Cretaceous AFT ages. Samples located in the Chinese Northern Tian Shan (Wang et al., 2009) were interpreted to have exhumed in response to the Kohistan-Dras arc collision, while samples in the easternmost section of the Chinese Tian Shan (Gillespie et al., 2017a) were associated with ongoing tectonic processes following the formation of the MOOB. In the Kyrgyz Northern Tian Shan, De Grave et al. (2013) linked samples to be recording the far-field effects of the Karakoram collision. Here, we demonstrate that the Late Cretaceous cooling ages follow the same 'boomerang' trend as recorded by other data in the study area (Fig. 6) and, therefore, can simply be interpreted in terms of a continuation of the rapid Early Cretaceous cooling event. In fact, very long (above 13.5 μm) MTLs (Fig. 6) and associated more rapid cooling histories reported in (De Pelsmaeker et al., 2015), may suggest that the Early Cretaceous cooling ages still reflect some inheritance of an older thermal event and, therefore, the timing of the cooling event may be more accurately constrained by the start of the Late Cretaceous. This timing is more in-line with previous studies, where fault reactivation was constrained to ~120–100 Ma throughout Central Asia (e.g. Glorie et al., 2012a, b; Gillespie et al., 2017a, b; Jepson et al., 2018b).

6. Conclusions

The thermochronological results for the Junggar Alatau preserve a complex cooling history:

(1) Late Carboniferous-Late Permian (~320–250 Ma) cooling ages are preserved in areas away from the main structures that dissect the Junggar Alatau. These cooling ages can be linked to the closure of the Palaeo-Asian Ocean.
(2) The study area reports only limited evidenced for Late Triassic–Early Jurassic (~230–190 Ma) cooling, which can be attributed to the Qiangtang collision. While such cooling signal is widely observed throughout the Tian Shan (particularly in stable, low-relief areas), the Junggar Alatau was either not strongly affected by the far-field stresses related to this tectonic event, or the thermochronological record for this event was largely erased by subsequent overprints.
(3) The most prominent, Early to early Late Cretaceous cooling phase was recorded localised along the Central Kazakhstan Fault Zone that dissects the study area. This cooling phase is interpreted in terms of exhumation by fault reactivation, associated with extensional/transtensional tectonics in response to slab-rollback of the subducting Tethys Ocean (~150–120 Ma).

Cenozoic exhumation in response to the India-Eurasia collision was not recorded in this study, indicating that the extent of stress-field propagation through the crustal architecture has not reached the Junggar Alatau at the extent where low-temperature thermochronological clocks would record this event.

Acknowledgements

This study was supported by an Australian Research Council Discovery Project (DP150101730), the National Key R & D Program of China (2017YFC0601206), and the National Natural Science Foundation of China (41888101). This is a contribution to IGCP 662 and forms TRaX record #417. S. Gilbert and other staff at Adelaide Microscopy are thanked for technical assistance in the laboratory. B. Ware and K. Rankenburg are thanked for help with solution ICP-MS analyses. I. Dunkl is thanked for sharing PepiFLEX software used for ICP-MS data reduction. Z. Martelli and A. Frew are thanked for help with sample preparation and supervision of He measurements. FZ his contribution was supported by the state assignment of IGM SB RAS. Two anonymous reviewers are thanked for their constructive comments and suggestions.

Appendix A. Supplementary data

Supplementary data to this article can be found online at https://doi.org/10.1016/j.gsf.2019.05.005.

References

Bande, A., Sobel, E.R., Mikolaichuk, A., Schmidt, A., Stockli, D.F., 2017. Exhumation history of the western Kyrgyz Tien Shan: implications for intramontane basin formation. Tectonics 36, 163–180.

Bande, A., Sobel, E.R., Mikolaichuk, A., Torres Acosta, V., 2015. Talas–fergana fault cenozoic timing of deformation and its relation to pamir indentation. Geol. Soc., Lond., Spec. Publ. 427. SP427.421.

Blackbourn, G., 2015. The Petroleum geology of Kazakhstan. Search Discov. J. Article #10711.

Brunet, M.F., Sobel, E.R., McCann, T., 2017. Geological evolution of central asian basins and the western Tien Shan range. Geol. Soc., Lond., Spec. Publ. 427, 1–17.

Bullen, M.E., Burbank, D.W., Garver, J.I., Abdrakhmatov, K.Y., 2001. Late Cenozoic tectonic evolution of the northwestern Tien Shan: new age estimates for the initiation of mountain building. Geol. Soc. Am. Bull. 113, 1544–1559.

Buvalkin, 1978. Jurassic Deposits of the East Kazakhstan (Paleogeograpy, Paleotectonic and Coal Contents). Alma-Ata: Nauka, p. 165.

Chew, D.M., Petrus, J.A., Kamber, B.S., 2014. U–Pb LA–ICPMS dating using accessory mineral standards with variable common Pb. Chem. Geol. 363, 185–199.

Chew, D.M., Spikings, R.A., 2015. Geochronology and thermochronology using apatite: time and temperature, lower crust to surface. Elements 11, 189–194.

Choulet, F., Chen, Y., Cogne, J.P., Rabillard, A., Wang, B., Lin, W., Faure, M., Cluzel, D., 2013. First triassic palaeomagnetic constraints from Junggar (NW China) and their implications for the Mesozoic tectonics in central Asia. J. Asian Earth Sci. 78, 371–394.

Choulet, F., Faure, M., Cluzel, D., Chen, Y., Lin, W., Wang, B., 2012. From oblique accretion to transpression in the evolution of the Altaid collage: new insights from West Junggar, northwestern China. Gondwana Res. 21, 530–547.

Danisik, M., Evans, N.J., Ramanaidou, E.R., McDonald, B.J., Mayers, C., McInnes, B.I.A., 2013. (U-Th)/He chronology of the Robe River channel iron deposits, Hamersley Province, western Australia. Chem. Geol. 354, 150–162.

De Grave, J., Buslov, M.M., Van den Haute, P., 2007. Distant effects of India-Eurasia convergence and Mesozoic intracontinental deformation in Central Asia: constraints from apatite fission-track thermochronology. J. Asian Earth Sci. 29, 188–204.

De Grave, J., De Pelsmaeker, E., Zhimulev, F.I., Glorie, S., Buslov, M.M., Van den Haute, P., 2014. Meso-Cenozoic building of the northern central Asian orogenic belt: thermotectonic history of the tuva region. Tectonophysics 621, 44–59.

De Grave, J., Glorie, S., Buslov, M.M., Izmer, A., Fournier-Carrie, A., Batalev, V.Y., Vanhaecke, F., Elburg, M., Van den haute, P., 2011. The thermo-tectonic history of the Song-Kul plateau, Kyrgyz Tien Shan: constraints by apatite and titanite thermochronometry and zircon U/Pb dating. Gondwana Res. 20, 745–763.

De Grave, J., Glorie, S., Buslov, M.M., Stockli, D.F., McWilliams, M.O., Batalev, V.Y., Van den haute, P., 2013. Thermo-tectonic history of the Issyk-Kul basement (Kyrgyz Northern Tien Shan, Central Asia). Gondwana Res. 23, 998–1020.

De Grave, J., Glorie, S., Ryabinin, A., Zhimulev, F., Buslov, M.M., Izmer, A., Elburg, M., Vanhaecke, F., Van den haute, P., 2012. Late Palaeozoic and Meso-Cenozoic tectonic evolution of the southern Kyrgyz Tien Shan: constraints from multi-method thermochronology in the Trans-Alai, Turkestan-Alai segment and the southeastern Ferghana Basin. J. Asian Earth Sci. 44, 149–168.

De Grave, J., Van den haute, P., 2002. Denudation and cooling of the Lake Teletskoye Region in the Altai Mountains (South Siberia) as revealed by apatite fission-track thermochronology. Tectonophysics 349, 145–159.

De Grave, J., Van den Haute, P., Buslov, M.M., Dehandschutter, B., Glorie, S., 2008. Apatite fission-track thermochronology applied to the Chulyshman Plateau, Siberian Altai Region. Radiat. Measurem. 43, 38–42.

De Pelsmaeker, E., Glorie, S., Buslov, M.M., Zhimulev, F.I., Poujol, M., Korobkin, V.V., Vanhaecke, F., Vetrov, E.V., De Grave, J., 2015. Late-Paleozoic emplacement and Meso-Cenozoic reactivation of the southern Kazakhstan granitoid basement. Tectonophysics 662, 416–433.

De Pelsmaeker, E., Jolivet, M., Laborde, A., Poujol, M., Robin, C., Zhimulev, F.I., Nachtergaele, S., Glorie, S., De Clercq, S., Batalev, V.Y., De Grave, J., 2018. Source-to-sink dynamics in the Kyrgyz Tien Shan from the Jurassic to the Paleogene: insights from sedimentological and detrital zircon U-Pb analyses. Gondwana Res. 54, 180–204.

Du, Z., Wang, Q., Zhou, X., 2007. Mesozoic and Cenozoic uplifting history of the Kuqa-South Tianshan Basin-Mountain System from the evidence of apatite fission track analysis. Acta Petrol. Mineral. 26, 399–408.

Dumitru, T.A., Zhou, D., Z, C.E., Graham, S.A., Hendrix, M.S., Sobel, E.R., Carroll, A.R., 2001. Uplift, exhumation, and deformation in the Chinese Tian Shan. Geological Society of America Memoir 194, 71–99.

Ehlers, T.A., Farley, K.A., 2003. Apatite (U-Th)/He thermochronometry: methods and applications to problems in tectonic and surface processes. Earth Planet. Sci. Lett. 206, 1–14.

Fernie, N., Glorie, S., Jessell, M.W., Collins, A.S., 2018. Thermochronological insights into reactivation of a continental shear zone in response to Equatorial Atlantic rifting (northern Ghana). Sci. Rep. 8 (1), 16619.

Flowers, R.M., Farley, K.A., Ketcham, R.A., 2015. A reporting protocol for thermochronologic modeling illustrated with data from the Grand Canyon. Earth Planet. Sci. Lett. 432, 425–435.

Gallagher, K., 2012. Transdimensional inverse thermal history modeling for quantitative thermochronology. J. Geophys. Res.: Solid Earth 117, B02408.

Gallagher, K., Brown, R., Johnson, C., 1998. Fission track analysis and its applications to geological problems. Ann. Rev. Earth Planet. Sci. 26, 519–572.

Gillespie, J., Glorie, S., Jepson, G., Zhang, Z.Y., Xiao, W.J., Danišík, M., Collins, A.S., 2017a. Differential exhumation and crustal tilting in the easternmost Tianshan (Xinjiang, China), revealed by low-temperature thermochronology. Tectonics 36, 2142–2158.

Gillespie, J., Glorie, S., Khudoley, A., Collins, A.S., 2018. Detrital apatite U-Pb and trace element analysis as a provenance tool: insights from the Yenisey Ridge (Siberia). Lithos 314, 140–155.

Gillespie, J., Glorie, S., Xiao, W.J., Zhang, Z.Y., Collins, A.S., Evans, N., McInnes, B., De Grave, J., 2017b. Mesozoic reactivation of the Beishan, southern Central Asian Orogenic Belt: insights from low-temperature thermochronology. Gondwana Res. 43, 107–122.

Glorie, S., Agostino, K., Dutch, R., Pawley, M., Hall, J., Danisik, M., Evans, N.J., Collins, A.S., 2017a. Thermal history and differential exhumation across the Eastern Musgrave Province, South Australia: insights from low-temperature thermochronology. Tectonophysics 703, 23–41.

Glorie, S., Alexandrov, I., Nixon, A., Jepson, G., Gillespie, J., Jahn, B.-M., 2017b. Thermal and exhumation history of Sakhalin Island (Russia) constrained by apatite U-Pb and fission track thermochronology. J. Asian Earth Sci. 143, 326–342.

Glorie, S., De Grave, J., 2016. Exhuming the Meso–Cenozoic Kyrgyz Tianshan and Siberian Altai-Sayan: a review based on low-temperature thermochronology. Geosci. Front. 7, 155–170.

Glorie, S., De Grave, J., Buslov, M.M., Elburg, M.A., Stockli, D.F., Gerdes, A., Van den haute, P., 2010. Multi-method chronometric constraints on the evolution of the northern Kyrgyz Tien Shan granitoids (central asian orogenic belt): from emplacement to exhumation. J. Asian Earth Sci. 38, 131–146.

Glorie, S., De Grave, J., Buslov, M.M., Zhimulev, F.I., Elburg, M.A., Van den Haute, P., 2012a. Structural control on Meso-Cenozoic tectonic reactivation and denudation in the Siberian Altai: insights from multi-method thermochronometry. Tectonophysics 544, 75–92.

Glorie, S., De Grave, J., Buslov, M.M., Zhimulev, F.I., Stockli, D.F., Batalev, V.Y., Izmer, A., Van den haute, P., Vanhaecke, F., Elburg, M.A., 2011. Tectonic history of the Kyrgyz South Tien Shan (Atbashi-Inylchek) suture zone: the role of inherited structures during deformation-propagation. Tectonics 30, TC6016.

Glorie, S., De Grave, J., Delvaux, D., Buslov, M.M., Zhimulev, F.I., Vanhaecke, F., Elburg, M.A., Van den haute, P., 2012b. Tectonic history of the Irtysh shear zone (NE Kazakhstan): new constraints from zircon U/Pb dating, apatite fission track dating and palaeostress analysis. J. Asian Earth Sci. 45, 138–149.

Glorie, S., Jepson, G., Konopelko, D., Mirkamalov, R., Meeuws, F., Gilbert, S., Gillespie, J., Collins, A.S., Xiao, W., Dewaele, S., De Grave, J., 2019. Thermochronological and geochemical footprints of post-orogenic fluid alteration recorded in apatite: implications for mineralisation in the Uzbek Tian Shan. Gondwana Res. 71, 1–15.

Green, P.F., 1986. On the thermo-tectonic evolution of Northern England: evidence from fission track analysis. Geol. Mag. 123, 493–506.

Guo, Z., Fang, S., Zhang, R., Zhang, Z., Wu, C., Shao, K., 2006. Growth strata and their application in timing deformation of foreland thrust-fold belts in the north margin of Tianshan. Oil & Gas Geol. 27, 475–481.

Han, Y., Zhao, G., 2018. Final amalgamation of the Tianshan and Junggar orogenic collage in the southwestern Central Asian Orogenic Belt: constraints on the closure of the Paleo-Asian Ocean. Earth-Sci. Rev. 186, 129–152.

Hendrix, M.S., Dumitru, T.A., Graham, S.A., 1994. Late Oligocene-early Miocene unroofing in the Chinese Tian Shan: an early effect of the India-Asia collision. Geology 22, 487–490.

Hendrix, M.S., Graham, S.A., Carroll, A.R., Sobel, E., Mcknight, C.L., Schulein, B.J., Wang, Z., 1992. Sedimentary record and climatic implications of recurrent deformation in the Tian Shan: evidence from Mesozoic strata of the north Tarim, south Junggar, and Turpan basins, northwest China. Geolog. Soc. Am. Bull. 104, 53–79.

Huang, H., Cawood, P.A., Ni, S., Hou, M., Shi, Z., Hu, X., 2017. Provenance of late Paleozoic strata in the Yili Basin: implications for tectonic evolution of the South Tianshan orogenic belt. GSA Bull. 130, 952–974.

Jepson, G., Glorie, S., Khudoley, A.K., Malyshev, S.V., Alexeiev, D.V., Glasmacher, U.A., Collins, A.S., 2019. The Mesozoic thermo-tectonic evolution of the Karatau and Talas ranges, Kazakh and Kyrgyz Tian Shan. Geol. J. (in review).

Jepson, G., Glorie, S., Konopelko, D., Gillespie, J., Danisik, M., Evans, N.J., Mamadjanov, Y., Collins, A.S., 2018a. Thermochronological insights into the structural contact between the Tian Shan and Pamirs, Tajikistan. Terra Nova 30, 95–104.

Jepson, G., Glorie, S., Konopelko, D., Gillespie, J., Danisik, M., Mirkamalov, R., Mamadjanov, Y., Collins, A.S., 2018b. Low-temperature thermochronology of the Chatkal-Kurama terrane (Uzbekistan-Tajikistan): insights into the Meso-Cenozoic thermal history of the western Tian Shan. Tectonics 37, 3954–3969.

Jepson, G., Glorie, S., Konopelko, D., Mirkamalov, R., Danišík, M., Collins, A.S., 2018c. The low-temperature thermo-tectonic evolution of the western Tian Shan, Uzbekistan. Gondwana Res. 64, 122–136.

Jia, Y., Fu, B., Jolivet, M., Zheng, S., 2015. Cenozoic tectono-geomorphological growth of the SW Chinese Tian Shan: insight from AFT and detrital zircon U–Pb data. J. Asian Earth Sci. 111, 395–413.

Jolivet, M., Brunel, M., Seward, D., Xu, Z., Yang, J., Roger, F., Tapponnier, P., Malavieille, J., Arnaud, N., Wu, C., 2001. Mesozoic and Cenozoic tectonics of the northern edge of the Tibetan plateau: fission-track constraints. Tectonophysics 343, 111–134.

Jolivet, M., De Boisgrollier, T., Petit, C., Fournier, M., Sankov, V.A., Ringenbach, J.C., Byzov, L., Miroshnichenko, A.I., Kovalenko, S.N., Anisimova, S.V., 2009. How old is the Baikal Rift Zone? Insight from apatite fission track thermochronology. Tectonics 28, TC3008.

Jolivet, M., Dominguez, S., Charreau, J., Chen, Y., Li, Y., Wang, Q., 2010. Mesozoic and Cenozoic tectonic history of the central Chinese Tian Shan: reactivated tectonic structures and active deformation. Tectonics 29, TC6019.

Jolivet, M., Ritz, J.-F.o., Vassallo, R., Larroque, C., Braucher, R.g., Todbileg, M., Chauvet, A., Sue, C., Arnaud, N., De Vicente, R., Arzhanikova, A., Arzhanikov, S., 2007. Mongolian summits: an uplifted, flat, old but still preserved erosion surface. Geology 35, 871–874.

Käßner, A., Ratschbacher, L., Jonckheere, R., Enkelmann, E., Khan, J., Sonntag, B.L., Gloaguen, R., Gadoev, M., Oimahmadov, I., 2016. Cenozoic intracontinental deformation and exhumation at the northwestern tip of the India-Asia collision—southwestern Tian Shan, Tajikistan, and Kyrgyzstan. Tectonics 35, 2171–2194.

Korobkin, V.V., Buslov, M.M., 2011. Tectonics and geodynamics of the western Central Asian Fold Belt (Kazakhstan Paleozoides). Russ. Geol. Geophys. 52, 1600–1618.

Kröner, A., Alexeiev, D.V., Kovach, V.P., Rojas-Agramonte, Y., Tretyakov, A.A., Mikolaichuk, A.V., Xie, H., Sobel, E.R., 2017. Zircon ages, geochemistry and Nd isotopic systematics for the Palaeoproterozoic 2.3–1.8 Ga Kuilyu Complex, East Kyrgyzstan – the oldest continental basement fragment in the Tianshan orogenic belt. J. Asian Earth Sci. 135, 122–135.

Laurent-Charvet, S., Charvet, J., Monié, P., Shu, L., 2003. Late Paleozoic strike-slip shear zones in eastern central Asia (NW China): new structural and geochronological data. Tectonics 22, 1009.

Li, P., Sun, M., Rosenbaum, G., Jourdan, F., Li, S., Cai, K., 2017. Late Paleozoic closure of the Ob-Zaisan Ocean along the Irtysh shear zone (NW China): implications for arc amalgamation and oroclinal bending in the Central Asian orogenic belt. GSA Bull. 129, 547–569.

Li, P., Sun, M., Rosenbaum, G., Yuan, C., Safonova, I., Cai, K., Jiang, Y., Zhang, Y., 2018. Geometry, kinematics and tectonic models of the Kazakhstan orocline, central Asian orogenic belt. J. Asian Earth Sci. 153, 42–56.

Ma, L., Wang, Q., Li, Z.-X., Wyman, D.A., Jiang, Z.-Q., Yang, J.-H., Gou, G.-N., Guo, H.-F., 2013. Early Late Cretaceous (ca. 93Ma) norites and hornblendites in the Milin area, eastern Gangdese: lithosphere–asthenosphere interaction during slab roll-back and an insight into early Late Cretaceous (ca. 100–80Ma) magmatic "flare-up" in southern Lhasa (Tibet). Lithos 172–173, 17–30.

Macaulay, E.A., Sobel, E.R., Mikolaichuk, A., Kohn, B., Stuart, F.M., 2014. Cenozoic deformation and exhumation history of the Central Kyrgyz Tien Shan. Tectonics 33, 135–165.

Martinson, G.G., Khomutova, V.I., Drabkova, V.G., 1983. Paleolimnological investigations in humid and arid zones of the Soviet Union. Hydrobiologia 103 (1), 257–260. https://doi.org/10.1007/BF00028462.

McDannell, K.T., Zeitler, P.K., Idleman, B.D., 2018. Relict topography within the Hangay mountains in Central Mongolia: quantifying long-term exhumation and relief change in an old landscape. Tectonics 37, 2531–2558.

McDowell, F.W., McIntosh, W.C., Farley, K.A., 2005. A precise $^{40}Ar-^{39}Ar$ reference age for the Durango apatite (U–Th)/He and fission-track dating standard. Chem. Geol. 214, 249–263.

Metelkin, D.V., Vernikovsky, V.A., Kazansky, A.Y., 2012. Tectonic evolution of the Siberian paleocontinent from the Neoproterozoic to the Late Mesozoic: paleomagnetic record and reconstructions. Russ. Geol. Geophys. 53, 675–688.

Metelkin, D.V., Vernikovsky, V.A., Kazansky, A.Y., Wingate, M.T.D., 2010. Late Mesozoic tectonics of Central Asia based on paleomagnetic evidence. Gondwana Res. 18, 400–419.

Mohadjer, S., Strube, T., Ehlers, T.A., Bendick, R., 2015. Central Asia Fault Database [ONLINE] Available at: esdynamics.geo.uni-tuebingen.de/faults/ [02/05/19].

Nachtergaele, S., De Pelsmaeker, E., Glorie, S., Zhimulev, F., Jolivet, M., Danišík, M., Buslov, M.M., De Grave, J., 2018. Meso-Cenozoic tectonic evolution of the Talas-Fergana region of the Kyrgyz Tien Shan revealed by low-temperature basement and detrital thermochronology. Geosci. Front. 9, 1495–1514.

Novikov, I.S., 2013. Reconstructing the stages of orogeny around the Junggar basin from the lithostratigraphy of Late Paleozoic, Mesozoic, and Cenozoic sediments. Rus. Geol. Geophys. 54, 138–152.

Paton, C., Hellstrom, J., Paul, B., Woodhead, J., Hergt, J., 2011. Iolite: freeware for the visualisation and processing of mass spectrometric data. J. Anal. Atom. Spectrom. 26, 2508–2518.

Petrov, O., Pospelov, I.I., Shokalsky, S., Tolmacheva, T.Y., Kashubin, S., 2016. Atlas of Geological Maps of Asia and Adjacent Areas. VSEGEI Publishing House, p. 48.

Rutte, D., Ratschbacher, L., Khan, J., Stubner, K., Hacker, B.R., Stearns, M.A., Enkelmann, E., Jonckheere, R., Pfander, J.A., Sperner, B., Tichomirowa, M., 2017. Building the Pamir-Tibetan PlateauCrustal stacking, extensional collapse, and lateral extrusion in the Central Pamir: 2. Timing and rates. Tectonics 36, 385–419.

Sobel, E.R., Chen, J., Heermance, R.V., 2006a. Late Oligocene–early Miocene initiation of shortening in the southwestern Chinese Tian Shan: implications for Neogene shortening rate variations. Earth Planet. Sci. Lett. 247, 70–81.

Sobel, E.R., Dumitru, T.A., 1997. Thrusting and exhumation around the margins of the western Tarim basin during the India-Asia collision. J. Geophys. Res.-Solid Earth 102, 5043–5063.

Sobel, E.R., Oskin, M., Burbank, D.W., Mikolaichuk, A., 2006b. Exhumation of basement-cored uplifts: example of the Kyrgyz Range quantified with apatite fission track thermochronology. Tectonics 25.

Song, D., Glorie, S., Xiao, W., Collins, A.S., Gillespie, J., Jepson, G., Li, Y., 2018. Tectonothermal evolution of the southwestern Alxa Tectonic Belt, NW China: constrained by apatite U-Pb and fission track thermochronology. Tectonophysics 722, 577–594.

Stockli, D.F., 2005. Application of low-temperature thermochronometry to extensional tectonic settings. Rev. Mineral. Geochem. 58, 411–448.

Stockli, D.F., Farley, K.A., Dumitru, T.A., 2000. Calibration of the apatite (U-Th)/He thermochronometer on an exhumed fault block, White Mountains, California. Geology 28, 983–986.

Tang, W.H., Zhang, Z.C., Li, J.F., Li, K., Luo, Z.W., Chen, Y., 2015. Mesozoic and Cenozoic uplift and exhumation of the Bogda Mountain, NW China: evidence from apatite fission track analysis. Geosci. Front. 6, 617–625.

Van Hinsbergen, D.J., Lippert, P.C., Dupont-Nivet, G., McQuarrie, N., Doubrovine, P.V., Spakman, W., Torsvik, T.H., 2012. Greater India basin hypothesis and a two-stage Cenozoic collision between India and Asia. Proc. Nat. Acad. of Sci. 109, 7659–7664.

Venus, B.G., Verzilin, N.N., Kyansep-Romashkina, N.P., Mironenko, O.A., Tolstikova, N.V., P, S.V., S, S.E., S, S.N., M, C.V., 1980. Paleolimnology of Zaisan Leningrad, 10 (6), 183–196. https://doi.org/10.1016/j.gsf.2019.05.005.

Vermeesch, P., 2009. RadialPlotter: a Java application for fission track, luminescence and other radial plots. Rad. Measurem. 44, 409–410.

Vermeesch, P., 2017. Statistics for LA-ICP-MS based fission track dating. Chem. Geol. 456, 19–27.

Wagner, G.A., Gleadow, A.J.W., Fitzgerald, P.G., 1989. The significance of the partial annealing zone in apatite fission-track analysis: projected track length measurements and uplift chronology of the Transantarctic Mountains. Chem. Geosci. 79, 295–305.

Wang, Q., Li, S., Du, Z., 2009. Differential uplift of the Chinese Tianshan since the Cretaceous: constraints from sedimentary petrography and apatite fission-track dating. Int. J. Earth Sci. 98, 1341–1363.

Wang, X., Cai, K., Sun, M., Xiao, W., Xia, X., Wan, B., Bao, Z., Wang, Y., 2018a. Two contrasting late Paleozoic magmatic episodes in the northwestern Chinese Tianshan Belt, NW China: implication for tectonic transition from plate convergence to intra-plate adjustment during accretionary orogenesis. J. Asian Earth Sci. 153, 118–138.

Wang, Y.N., Cai, K.D., Sun, M., Xiao, W.J., De Grave, J., Wan, B., Bao, Z.H., 2018b. Tracking the multi-stage exhumation history of the western Chinese Tianshan by apatite fission track (AFT) dating: implication for the preservation of epithermal deposits in the ancient orogenic belt. Ore Geol. Rev.s 100, 111–132.

Windley, B.F., Alexeiev, D., Xiao, W., Kroener, A., Badarach, G., 2007. Tectonic models for accretion of the Central Asian Orogenic Belt. J. Geol. Soc. 164, 31–47.

Yang, W., Jolivet, M., Dupont-Nivet, G., Guo, Z.J., 2014. Mesozoic - Cenozoic tectonic evolution of southwestern Tian Shan: evidence from detrital zircon U/Pb and apatite fission track ages of the Ulugqat area, Northwest China. Gondwana Res. 26, 986–1008.

Yuan, W.M., Carter, A., Dong, J.Q., Bao, Z.K., An, Y.C., Guo, Z.J., 2006. Mesozoic-tertiary exhumation history of the Altai Mountains, northern Xinjiang, China: new constraints from apatite fission track data. Tectonophysics 412, 183–193.

Zahirovic, S., Matthews, K.J., Flament, N., Müller, R.D., Hill, K.C., Seton, M., Gurnis, M., 2016. Tectonic evolution and deep mantle structure of the eastern Tethys since the latest Jurassic. Earth-Sci. Rev. 162, 293–337.

Zhang, Z., Guo, Z., Wu, C., Fang, S., 2007. Thermal history of the Jurassic Strata in the Northern Tianshan and its geological significance, revealed by apatite fission-track and vitrinite reflectance analysis. Acta Petrol. Sin. 23, 1683–1695.

Zhang, Z., Zhu, W., Zheng, D., Zheng, B., Yang, W., 2016. Apatite fission track thermochronology in the Kuluketage and Aksu areas, NW China: implication for tectonic evolution of the northern Tarim. Geosci. Front. 7, 171–180.

Zhang, Z.Y., Zhu, W.B., Shu, L.S., Wan, J.L., Yang, W., Su, J.B., Zheng, B.H., 2009. Apatite fission track thermochronology of the Precambrian Aksu blueschist, NW China: implications for thermo-tectonic evolution of the north Tarim basement. Gondwana Res. 16, 182–188.

Zhao, L., He, G., 2013. Tectonic entities connection between west Junggar (NW China) and east Kazakhstan. J. Asian Earth Sci. 72, 25–32.

Zhu, X., Wang, B., Chen, Y., Liu, H., Horng, C.-s., Choulet, F., Faure, M., Shu, L., Xue, Z., 2018. First early Permian paleomagnetic Pole for the Yili block and its implications for late Paleozoic postorogenic kinematic evolution of the SW central Asian orogenic belt. Tectonics 37, 1709–1732.